Evidence for exotic $J^{PC}=1^{-+}$ meson production in the reaction $\pi^-p \to \eta\pi^-p$ at 18 GeV/c

S. U. Chung, K. Danyo, R. W. Hackenburg, C. Olchanski, D. P. Weygand,* and H. J. Willutzki

Department of Physics, Brookhaven National Laboratory, Upton, New York 11973

S. P. Denisov, V. A. Dorofeev, I. A. Kachaev, V. V. Lipaev, A. V. Popov, and D. I. Ryabchikov

Institute for High Energy Physics, Protvino, Russian Federation

Z. Bar-Yam, J. P. Dowd, P. Eugenio,† M. Hayek,‡ W. Kern, E. King, and N. Shenhav‡

Department of Physics, University of Massachusetts Dartmouth, North Dartmouth, Massachusetts 02747

V. A. Bodyagin, O. L. Kodolova, V. L. Korotkikh, M. A. Kostin, A. I. Ostrovidov, L. I. Sarycheva, N. B. Sinev, I. N. Vardanyan, and A. A. Yershov

Institute for Nuclear Physics, Moscow State University, Moscow, Russian Federation

D. S. Brown,§ T. K. Pedlar, K. K. Seth, J. Wise, and D. Zhao

Department of Physics, Northwestern University, Evanston, Illinois 60208

T. Adams,** J. M. Bishop, N. M. Cason, E. I. Ivanov, J. M. LoSecco, J. J. Manak,* A. H. Sanjari, W. D. Shephard, D. L. Stienike, S. A. Taegar,†† and D. R. Thompson

Department of Physics, University of Notre Dame, Notre Dame, Indiana 46556

G. S. Adams, J. P. Cummings, J. Kuhn, M. Nozar, J. A. Smith, D. B. White, and M. Witkowski

Department of Physics, Rensselaer Polytechnic Institute, Troy, New York 12180

(E852 Collaboration)

Details of the analysis of the $\eta\pi^-$ system studied in the reaction $\pi^-p \to \eta\pi^-p$ at 18 GeV/c are given. Separate analyses for the 2γ and $\pi^+\pi^-\pi^0$ decay modes of the η are presented. An amplitude analysis of the data indicates the presence of interference between the $a_2^-(1320)$ and a $J^{PC}=1^{-+}$ wave between 1.2 and 1.6 GeV/c^2. The phase difference between these waves shows a phase motion not attributable solely to the $a_2^-(1320)$. The data can be fitted by interference between the $a_2^-(1320)$ and an exotic 1^{-+} resonance with $M=(1370\pm16^{+50}_{-30})$ MeV/c^2 and $\Gamma=(385\pm40^{+65}_{-105})$ MeV/c^2. Our results are compared with those of other experiments. [S0556-2821(99)06119-6]

PACS number(s): 13.85.Fb, 12.39.Mk, 14.40.Cs

I. INTRODUCTION

In a previous publication [1], evidence was presented for an exotic meson produced in the reaction

$$\pi^-p \to \eta\pi^-p \qquad (1)$$

at 18 GeV/c, with the decay mode $\eta \to \gamma\gamma$. The purpose of this paper is to provide details of that analysis, to discuss additional analyses of those data, and to give a detailed comparison of our results with those of other experiments. We also compare those results with data from our experiment on Reaction (1) but with the $\eta \to \pi^+\pi^-\pi^0$ decay.

The $\eta\pi$ system is particularly interesting in searching for exotic (or non-$q\bar{q}$) mesons because the system has spin (J), parity (P), and charge-conjugation (C) in the sequence $J^{PC} = 0^{++}, 1^{-+}, 2^{++}, 3^{-+}, \ldots$ for $l=0,1,2,3,\ldots$. (Here l is the orbital angular momentum of the $\eta\pi$ system.) Hence a resonance with an $\eta\pi$ decay mode with odd l is manifestly exotic.[1] Having isospin $I=1$, such a resonance could not be a glueball ($2g,3g,\ldots$), but it could be a hybrid ($q\bar{q}g$) or a multiquark ($q\bar{q}q\bar{q}$) state.

_____

*Present address: Thomas Jefferson National Accelerator Facility, Newport News, VA 23606.

†Present address: Department of Physics, Carnegie Mellon University, Pittsburgh, PA 15213.

‡Permanent address: Rafael, Haifa, Israel.

§Present address: Department of Physics, University of Maryland, College Park, MD 20742.

**Present address: Department of Physics, Kansas State University, Manhattan, KS 66506.

††Present address: Department of Physics, University of Arizona, Tucson, AZ 85721.

_____

[1]A $q\bar{q}$ meson with orbital angular momentum L and total spin S must have $P=(-1)^{L+1}$ and the neutral member of its isospin multiplet must have $C=(-1)^{L+S}$. A resonance with quantum number in the sequence $J^{PC}=0^{--},0^{+-},1^{-+},2^{+-},3^{-+}\ldots$ does not satisfy these conditions and must be exotic.

A. Models

Properties of hybrids and multiquark mesons have been discussed in the framework of various models [2–12]. Calculations based upon the MIT bag model predict [3–6] that an $I=1, 1^{-+}$ hybrid ($q\bar{q}g$) will have a mass near 1.4 GeV/c^2. On the other hand, the flux-tube model [7,8] predicts the mass of the lowest-lying hybrid state to be around 1.8 GeV/c^2. Characteristics of bag-model S-wave multiquark states (which would have $J^P=0^+$, 1^+ or 2^+) have been discussed [9] but those for a 1^- state have not. QCD sum-rule predictions [10] vary widely between 1.0 GeV/c^2 and 2.5 GeV/c^2. Recently, an analysis of the multiquark hybrids has been carried out, based on the diquark cluster model [11]; this model predicts a lowest-lying isovector $J^{PC}=1^{-+}$ state at 1.39 GeV/c^2 with a very narrow width ($\simeq 8$ MeV/c^2). Finally, recent lattice-gauge calculations yield mass estimates for a 1^{-+} hybrid in the range from 1.7 to 2.1 GeV/c^2 [12].

B. Previous experiments

Several experiments, prior to the publication of the E852 results [1], had studied the $\eta\pi$ final state, and observed an enhancement in the P wave around 1400 MeV/c^2 [13–16]. However, they reached conflicting conclusions.

The 1988 GAMS experiment [13] at CERN ($\pi^- p$ at 100 GeV/c) claimed to find a narrow enhancement in the unnatural parity exchange P_0 wave, but found the natural parity exchange P_+ wave to be "structureless." The method of analysis and the conclusions were seriously disputed by some of the same authors later [17].

The 1993 VES experiment [14] at Serpukhov ($\pi^- N$ at 37 GeV/c on a beryllium target) found an enhancement in the natural parity exchange P_+ wave and concluded that "the P_+ wave is small but statistically significant and contains a broad bump." They made no attempt to identify the "bump" with a resonance.

The 1993 KEK experiment [15] ($\pi^- p$ at 6.3 GeV/c) claimed that "A clear enhancement of the P_+ wave was observed around 1.3 GeV/c^2" but noted that "The phase of the P_+ wave relative to the D_+ wave shows no distinct variation with mass in the analysis region." They therefore made no attempt to offer a resonance hypothesis.

The 1994 Crystal Barrel experiment [16] on $\bar{p}p$ annihilation at rest concluded that their "$\pi^0\pi^0\eta$ data may at most accommodate a small amount of featureless $\pi\eta$ P-wave."

The first claim for a 1^{-+} exotic resonance in the $\eta\pi^-$ channel was made by our experiment at BNL [1]. In this paper we present details of the measurements and method of analysis used in that earlier publication. We note that since the publication, an independent confirmation of our results has come from a new measurement by the Crystal Barrel Collaboration [18].

II. EXPERIMENTAL DETAILS

A. E852 apparatus

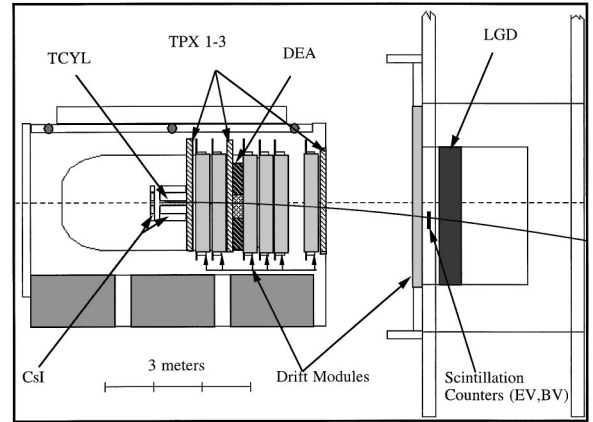Our data sample was collected in the first data run of E852 at the Alternating Gradient Synchrotron (AGS) at

FIG. 1. Experimental layout for E852. The nomenclature is defined in the text.

Brookhaven National Laboratory (BNL) with the Multi-Particle Spectrometer (MPS) [19] augmented by additional detectors. A diagram of the experimental apparatus is shown in Fig. 1. A Čerenkov tagged π^- beam of momentum 18 GeV/c was incident on a one-foot long liquid hydrogen target at the center of the MPS magnet. The target was surrounded by a four-layer cylindrical drift chamber (TCYL) [20] used to trigger on the proton recoil of Reaction (1), and a 198-element cylindrical thallium-doped cesium iodide array (CsI) [21] capable of rejecting events with wide-angle photons. The downstream half of the magnet was equipped with six drift chamber modules (DC1-6) [22], each consisting of seven planes, used for charged-particle tracking. Interspersed among these were three proportional wire chambers (TPX1-3) to allow triggering on the multiplicity of forward tracks; a window-frame lead scintillator photon veto counter (DEA) to ensure photon hermeticity; a scintillation counter (CPVB) to veto forward charged tracks for neutral triggers; and a window-frame scintillation counter (CPVC) to identify charged particles entering the DEA. Beyond the magnet were a newly-built drift chamber (TDX4) consisting of two x-planes; two scintillation counters (BV and EV) to veto non-interacting beam tracks and elastic scatters respectively; and a 3045-element lead glass electromagnetic calorimeter (LGD) [23] to detect forward photons. Further details are given elsewhere [24].

B. Trigger

The trigger (see Ref. [24] for details) for Reaction (1) required a recoil charged particle in the TCYL detector and one charged particle traversing each of the first two TPX chambers. In addition, an electronic algorithm [23] coupling energy and position information in the LGD calorimeter (an "effective-mass" trigger) was utilized for the purpose of enhancing the fraction of η's relative to π^0's in the sample. A total of 47 million triggers of this type were recorded.

C. Event reconstruction and selection

Of the 47 million triggers, 47,235 events were reconstructed which were consistent with Reaction (1). These

TABLE I. Reduction in the data sample as a function of the cut type.

Cut	Remaining number of events	Fraction removed (%)
Number of triggers	47×10^6	-
Topological and trigger cuts	583,094	98.8
η preselection (C.L.$>10^{-4}$)	270,364	53.6
Removal of runs with LGD trigger processor failure	159,871	40.9
LGD fiducial cut	146,584	8.3
Photon-hadron distance cut	145,710	0.60
Missing-mass-squared cut	103,341	29.1
Confidence level cut	85,888	16.9
$\Delta\phi<8°$	53,219	38.0
TPX2 cut	49,113	7.7
Cut on position at EV/BV	47,235	3.8
$0.10<|t|<0.95\,(\mathrm{GeV}/c^2)$	42,676	9.7
$0.98<M(\eta\pi^-)<1.85$ GeV/c^2	38,272	10.3

were selected by requiring:

topological and trigger cuts including requirements for

(1) two photons reconstructed in the LGD,
(2) one forward track reconstructed in DC1-6,
(3) one recoil track reconstructed in TCYL,
(4) a common vertex, in a target fiducial volume, reconstructed from the charged tracks and the beam track,
(5) no energy deposited in the DEA detector or outside the fiducial volume of the LGD,
(6) the energy deposited in the CsI array being less than 160 MeV;

that the effective mass of the two photons be consistent with the η effective mass with a confidence level greater than 10^{-4};
that all data come from runs which had proper functioning of the trigger processor;
that the photons hit the LGD within a fiducial volume which excluded a 4.0-cm region (one block width) around the periphery of the LGD as well as a 4.0-cm wide region surrounding the beam hole;
that the distance between a photon and a charged track hitting the LGD exceed 20 cm;
$-1.0<(\mathrm{missing\ mass})^2<2.5\,(\mathrm{GeV}/c^2)^2$;
a SQUAW [25] kinematic fit (requiring energy and momentum conservation) to Reaction (1) with a confidence level $>10\%$;
that the difference in angle $\Delta\phi$ between the fitted proton direction and the measured track in TCYL be less than 8°;
the exclusion of events for which the π^- went through an insensitive region of TPX2;
the exclusion of events for which the π^- went through a small region surrounding the EV/BV veto counters. (Events which had a π^- in this region were sometimes vetoed, probably due to Čerenkov radiation in the EV or BV light pipes).

Shown in Table I is the effect on the data sample for each of these cuts. The last two cuts listed in the table were additional cuts made on the data to carry out the partial-wave analysis (PWA).
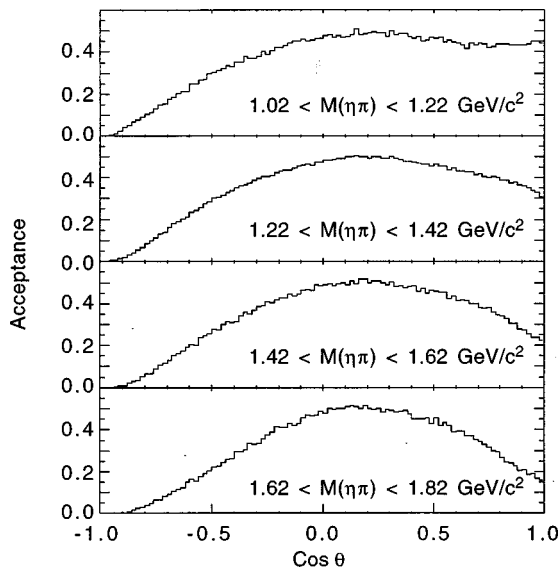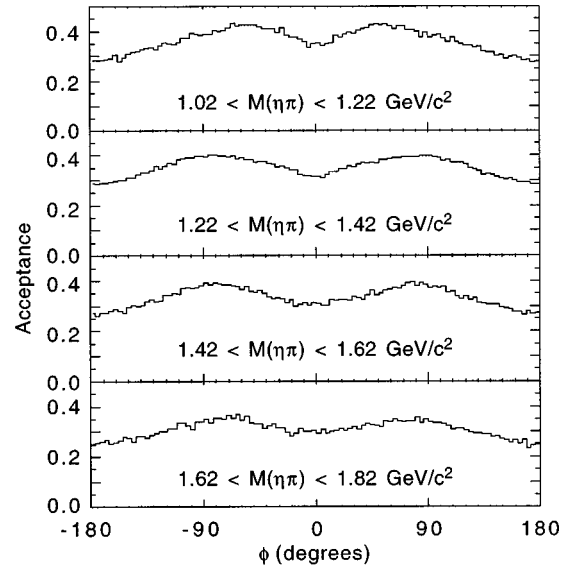
D. Experimental acceptance

The experimental acceptance is determined by a Monte Carlo method. Events are generated using SAGE [26] with peripheral production [of the form $dN/d|t|=A\exp-b|t|$ with $b=4.0\,(\mathrm{GeV}/c)^{-2}$] and with isotropic angular distributions in the Gottfried-Jackson (GJ) frame. (The GJ frame is a rest frame of the $\eta\pi^-$ system in which the z-axis is in the direction of the beam momentum, and the y-axis is in the direction of the vector cross-product of the target and recoil momenta.) After adding detector simulation using GEANT [27], the Monte Carlo event sample is subjected to the same event-selection cuts and run through the same analysis as the data. A second method (called SAGEN) which did not use GEANT was employed as well. This method also used SAGE as the event generator, but instead of using GEANT, the acceptance was determined using a full detector simulation but without such effects as multiple scattering, pair production and secondary interactions. This second method allowed acceptances to be calculated much more quickly. The only differences noted in the amplitude analysis results (discussed below) between the two methods was in the number of events, since GEANT takes account of pair production and secondary interactions, whereas SAGEN does not. The average acceptances are the ratios of the generated events to the accepted events and are shown in Figs. 2–4 using the SAGEN method.

The average acceptance as a function of $\eta\pi^-$ effective mass is shown in Fig. 2. The average acceptance decreases by about a factor of two over the effective mass region from 1.0 to 2.0 GeV/c^2. Average acceptances are calculated for peripheral production and isotropic decay as described above.
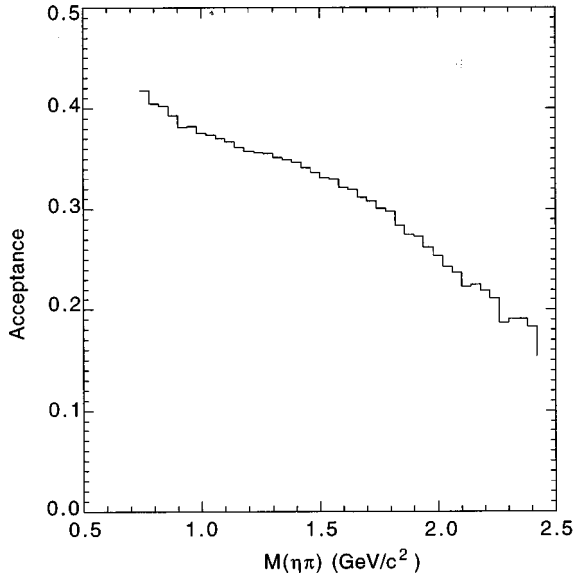
FIG. 2. Average acceptance vs. $\eta\pi^-$ effective mass.

FIG. 4. Average acceptance vs. ϕ for different $\eta\pi^-$ effective mass regions.

Shown in Figs. 3 and 4 is the acceptance as a function of $\cos\theta$ and of ϕ for various ranges of the $\eta\pi^-$ effective mass. Here θ and ϕ are the polar and azimuthal angles measured in the GJ frame. The polar angle is the angle between the beam direction and the η direction in this frame. The inefficiency in the backward direction corresponds to slow η's and fast π^-'s in the lab. The slow η's lead to low energy γ's which are often produced at wide angles and thus miss the LGD. In some cases, fast π^-'s cause the event to be vetoed if they strike the EV or BV scintillation counters, leading to further inefficiency in the backward direction. The inefficiency in the forward direction is due to an inefficiency in detecting slow, wide-angle pions which can scatter in the CsI detector. The acceptance in ϕ is relatively uniform. There is a corre-

lation between the energy of the η and ϕ at finite momentum transfer and this leads to the observed shape.

Finally, shown in Fig. 5 is the average acceptance (GEANT-based) as a function of $|t'|=|t-t_{min}|$, where t is the four-momentum-transfer between the initial- and final-state protons and t_{min} is the minimum value for this quantity for a given $\eta\pi^-$ effective mass. The dramatic decrease in acceptance below about $|t'|=0.08$ $(GeV/c)^2$ is due to a trigger requirement. In particular, since we require the presence of a recoil proton in TCYL, the trigger cannot be satisfied if the proton stops in the hydrogen target.

E. Background studies

Shown in Fig. 6 is the 2γ effective mass distribution for events in the $a_2^-(1320)$ mass region from 1.22 GeV/c^2 to 1.42 GeV/c^2. The data sample used for this distribution

FIG. 3. Average acceptance vs. $\cos\theta$ for different $\eta\pi^-$ effective mass regions.
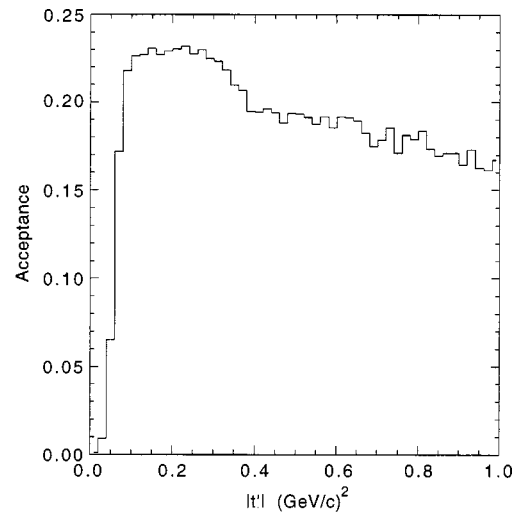
FIG. 5. Average acceptance vs. $|t'|$ integrated over all $\eta\pi^-$ effective masses.
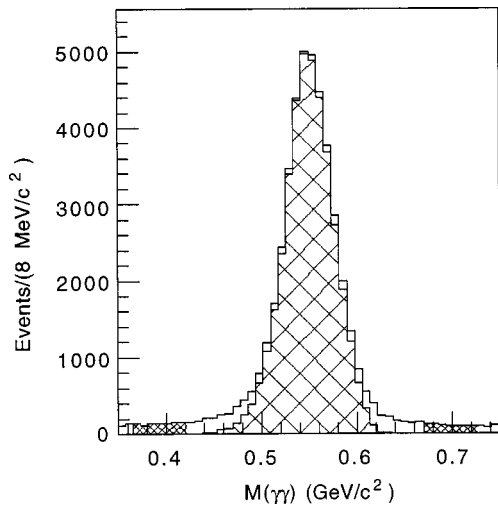
FIG. 6. Two-photon effective mass distribution for events in the $a_2^-(1320)$ effective-mass region. The central cross-hatched region shows the events which remain after SQUAW fitting. The shaded sidebands show the regions selected to estimate the background using Method 1 (see text).

FIG. 7. Missing-massed squared distribution. The dashed histogram shows the distribution of events which remain after kinematic fitting which leads to a rather sharp cutoff.

consisted of a subset of events satisfying the cuts listed in Table I but without SQUAW confidence level cuts. The central cross-hatched region in Fig. 6 shows the events which remain after the SQUAW-based kinematic-fitting cuts. The distribution has $\sigma \approx .03$ GeV/c^2. Both this distribution and the missing-mass-squared distribution discussed below are consistent with that expected from Monte Carlo studies when the energy resolution of the LGD for a photon of energy E is taken to be of the form $\sigma/E = a + b/\sqrt{E}$ with $a = 0.032$ and $b = .096$ (GeV)$^{1/2}$. (This was the resolution function used for the LGD in the kinematic fitting.) Two methods have been used to study the background in our sample. Method 1 used the shaded sidebands of Fig. 6 and allows us to study the non-η background in the data.

The missing-mass-squared distribution for the data sample before kinematic fitting is shown in Fig. 7. The dashed histogram shows the events which remain after kinematic fitting. The distribution for good events for Reaction (1) should peak at the square of the proton mass or at a value of 0.88 (GeV/c^2)^2.

A scatterplot of the missing-mass squared versus the 2γ effective mass is shown in Fig. 8. Background studies using our Method 2 take as the background estimator a region surrounding the central signal region seen here instead of using the sidebands of Fig. 6. In this way we take into account background events of both the non-η type and of the type which does have an η present but is not exclusively Reaction (1) such as events with an extra π^0. (The background is estimated using the region included within the outer elliptical area of Fig. 8 but not within the middle elliptical region. Events in this elliptical band are used to determine the magnitude of the background as a function of $\eta\pi$ effective mass.)

Shown in Fig. 9 is the effective-mass distribution of the background, estimated using Method 1. In this figure are shown the effective-mass distribution for each sideband region as well as the summed distribution for the background
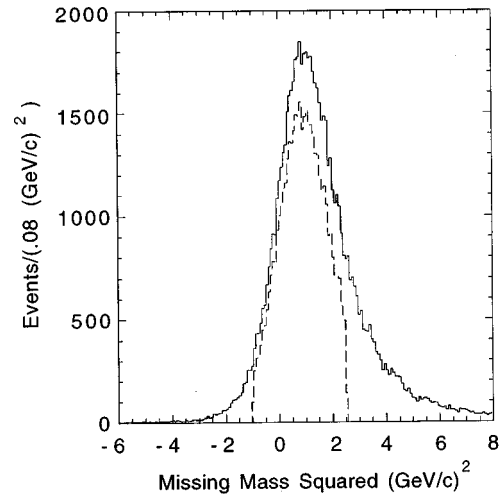
regions. Because the background regions have different thresholds, one higher than the signal region and one lower than the signal region, the histograms are shifted by an appropriate amount (so that their thresholds match that of the signal region) before summing.

In Fig. 10 is shown the polar angular distribution of the background events from Method 1 in the $a_2^-(1320)$ effective-mass region from 1.22 GeV/c^2 to 1.42 GeV/c^2. Distributions are shown separately for the low-mass and the high-mass sidebands of the η. This high-mass sideband distribution is somewhat peaked in the backwards direction with a tendency for the distribution to have an excess below the region $\cos\theta < -0.5$. We note that this is in the opposite direction from the asymmetry in the data (see below) and therefore cannot be the cause of the observed asymmetry. Of course the intensity of the background is quite small as seen
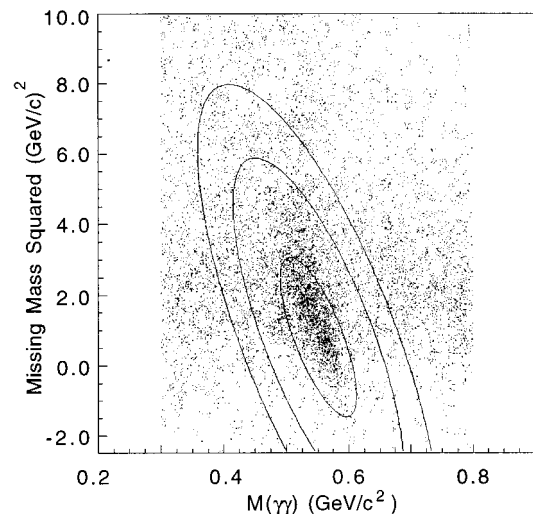

FIG. 8. Missing-mass squared vs. two-photon mass. The elliptical regions are used to estimate the background using Method 2 (see text).
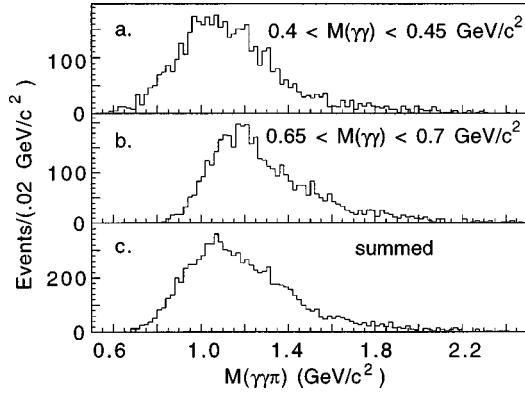
FIG. 9. Effective-mass distribution of the background estimated from the η sidebands (Method 1).

in Fig. 11 below and therefore could not lead to significant changes in the angular distributions in the data in any case.

III. GENERAL FEATURES OF THE DATA

The $a_2^-(1320)$ is the dominant feature of the $\eta\pi^-$ effective-mass spectrum shown in Fig. 11. The background, which is shown shaded in the figure, is estimated from Method 2 above, and is approximately 7% at 1.2 GeV/c^2, and only 1% at 1.3 GeV/c^2.

The acceptance-corrected distribution of $|t'|=|t-t_{\min}|$ is shown as the solid points in Fig. 12 for $|t'|$ >0.08 (GeV/c)^2. [Our acceptance is quite low below 0.08 (GeV/c)^2 as discussed in Sec. II D.] Since the data are dominated by $a_2^-(1320)$ production, we show as the solid curve (1) the prediction of a Regge role model for the differential cross section for the reaction $\pi^-p\rightarrow a_2^-p$ at 18 GeV/c. (Note that the ordinate values are given by the theory and the data are normalized to the theory so we are comparing only the shape of the data with the theoretical
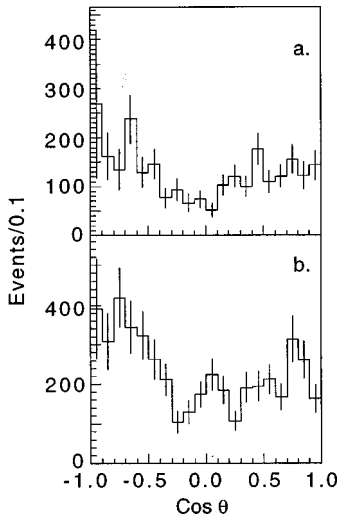

FIG. 10. Angular distribution of the background (Method 1) shown separately for (a) the low-mass sideband and (b) the high-mass sideband of the η. Events are plotted which fall in the $a_2^-(1320)$ effective-mass region.
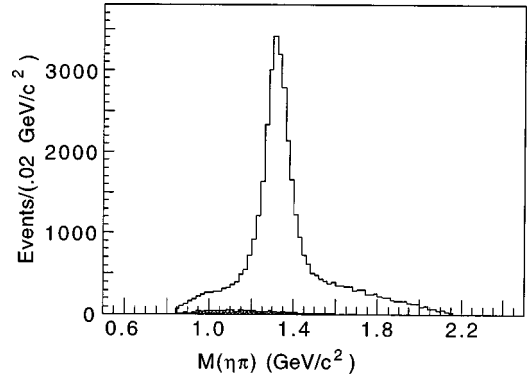

FIG. 11. $\eta\pi^-$ effective mass distribution uncorrected for acceptance. The shaded region is an estimate of the background using Method 2.

prediction.) The model includes contributions from ρ and f_2 Regge trajectories with parameters from a fit by Sacharidis [28] and also includes a small [4% at $t'=0.15$ (GeV/c)^2] contribution from a uniform (t' independent) background. For comparison, results of another experiment (open circles) [29] which studied the reaction $\pi^-p\rightarrow a_2^-p$, $a_2^-\rightarrow K^-K^0$ at 22.4 GeV/c and the Sacharidis fit (curve 2) are shown. (Note that the values shown take into account the a_2 decay branching fractions.) We conclude that the shape of our t' distribution is consistent with previous experiments and with natural-parity exchange production in Regge-pole phenomenology [30].

Acceptance-corrected distributions of $\cos\theta$ are shown in Fig. 13 for various ranges of $\eta\pi^-$ effective mass. For illustration purposes, the acceptance correction is calculated here for isotropic decay of the $\eta\pi^-$ system. The acceptance correction used in the amplitude analysis discussed below is based upon the observed decay angular distribution. The presence of a significant forward-backward asymmetry in the $\cos\theta$ distribution is obvious.

The forward-backward asymmetry in $\cos\theta$ is plotted as a function of $\eta\pi^-$ effective mass in Fig. 14. Here, the asym-
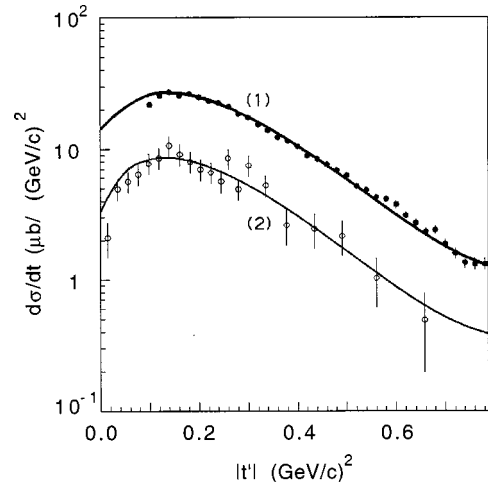

FIG. 12. Distribution of $|t'|=|t-t_{\min}|$ (acceptance-corrected). This experiment (solid dots) compared to a second experiment (open circles, see text) and to a Regge pole fit.
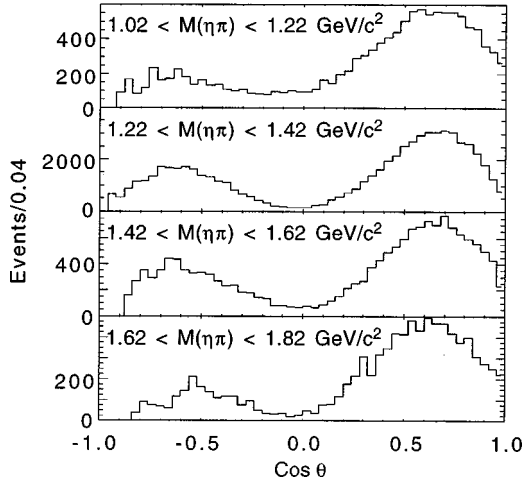
FIG. 13. Distributions of the acceptance-corrected cosine of the decay angle in the GJ frame for various effective mass selections.

metry is defined as $(F-B)/(F+B)$ where $F(B)$ is the number of events in the mass bin with the η decaying forward (backward) in the GJ frame. For this figure, the asymmetry was calculated for events in the region with $|\cos\theta| < 0.8$ to avoid any possibility of having results distorted by the extreme forward and backward regions which have low acceptance.[2] The asymmetry is large, statistically significant and mass dependent. Within the framework of the partial wave analysis discussed below, the presence of only even values of l would yield a symmetric distribution in $\cos\theta$. Thus the observed asymmetry requires that odd-l partial waves be present and that they interfere with even-l partial waves to describe the data. Note that the decrease in asymmetry in the 1.4 GeV/c^2 region can be (and will be shown to be) caused by the phase difference between the even-l and odd-l waves approaching $\pi/2$ rad.
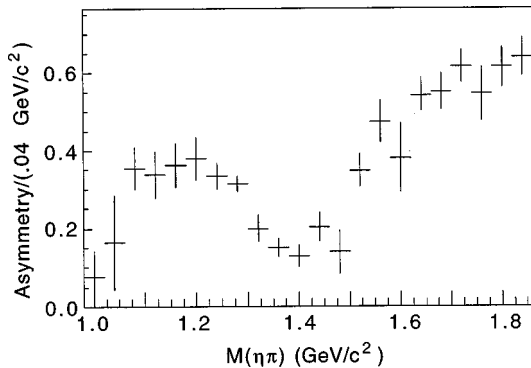

FIG. 14. Forward-backward asymmetry (acceptance-corrected) as a function of effective mass. The asymmetry $= (F-B)/(F+B)$ where $F(B)$ is the number of events for which the η decays in the forward (backward) hemisphere in the GJ frame.

---

[2]The asymmetry function was plotted for various ranges of the decay angle and the presence of a strong asymmetry was noted in all cases.
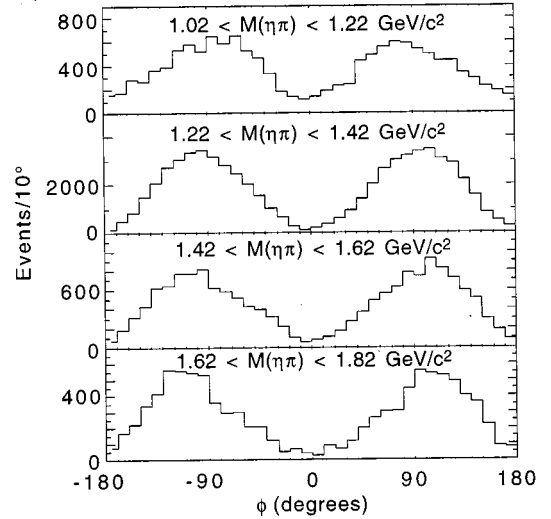

FIG. 15. Distributions of the acceptance-corrected Treiman-Yang angle ϕ in the GJ frame for various effective mass selections.

The azimuthal angular distribution as a function of $\eta\pi^-$ effective mass is shown in Fig. 15. The observed structure has a clear $\sin\phi$ component which indicates the presence of $m=1$ natural-parity-exchange waves in the production process. (See the discussion in Sec. IV below.)

Shown in Fig. 16 are the π^-p and ηp effective-mass distributions for the data sample. It is important to note that the absence of baryon isobar production is required for the assumptions of our PWA to be valid. There is at most a very small amount of isobar production in the region $M(\pi^-p) < 2.0$ GeV/c^2 in Fig. 16(a) and none in Fig. 16(b). The amplitude analysis described in Sec. IV was checked to ensure that isobar production did not effect our results. This was done by redoing that analysis after requiring $M(\pi^-p) > 2.0$ GeV/c^2. The resulting intensities and phases did not change (other than an overall magnitude change due to the loss of events) in most cases by more than one standard
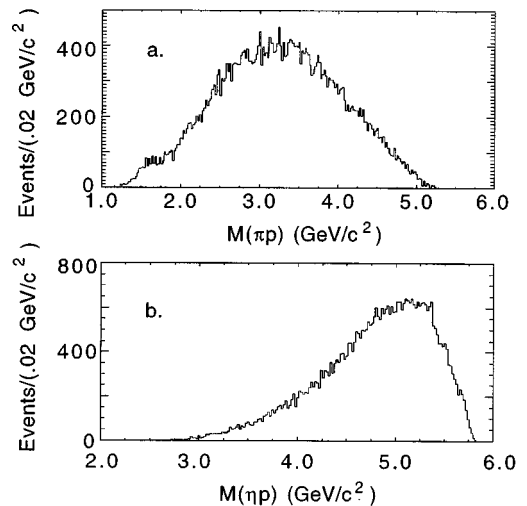

FIG. 16. Effective mass distributions for (a) the π^-p; and (b) the ηp systems for the final event sample (uncorrected).

deviation and in no case by more than 1.5 standard deviations.

IV. PARTIAL-WAVE ANALYSIS

A. Procedure

A partial-wave analysis (PWA) [31–33] based on the extended maximum likelihood method has been used to study the spin-parity structure of the $\eta\pi^-$ system. We give in Appendixes A and B some mathematical details regarding the techniques used in the partial-wave analysis. The formalism adopted in this analysis is somewhat different from those used by previous investigators. Although complete details used in the formalism are given in a recent publication by Chung [32], a portion of that work is reproduced in Appendixes A and B in order to make this paper as complete and self-contained as possible.

In Appendix A, a brief description of the formalism is given as the relationships between the partial wave amplitudes (assuming $l \leq 2$) and the moments of the angular distribution. The technique of the extended maximum likelihood analysis is covered in Appendix B, where the interplay of the experimental moments, Eq. (B1), and the acceptance is described. (The experimental acceptance is incorporated into the PWA by using the accepted Monte Carlo events described above to calculate normalization integrals—see Ref. [31].)

The partial waves are parametrized in terms of the quantum numbers J^{PC} as well as m, the absolute value of the angular momentum projection, and the reflectivity ϵ [34]. In our naming convention, a letter indicates the angular momentum of the partial wave in standard spectroscopic notation, while a subscript of 0 means $m=0$, $\epsilon=-1$, and a subscript of $+(-)$ means $m=1$, $\epsilon=+1(-1)$. Thus, S_0 denotes the partial wave having $J^{PC}m^\epsilon=0^{++}0^-$, while P_- signifies $1^{-+}1^-$, D_+ means $2^{++}1^+$, and so on.

We consider partial waves with $m \leq 1$ in our analysis. This assumption is true in the limit of $-t=0$, since the nucleon helicities give rise to the states with $m=0$ or $m=\pm 1$ only. But this assumption can be dealt with—experimentally—since the moments $H(LM)$ with $M=3$ or $M=4$ can be checked, to see how important the states $|lm\rangle$ are in the data with $|m| \geq 2$. This has been done with our data. The moments $H(33)$, $H(43)$ and $H(44)$ are all small in the $a_2^-(1320)$ region, and a fit including $|22\rangle$ (shown in Section IV C below) contains only a very small amount of this wave and is very broad.

We also assume that the production spin-density matrix has rank one. This assumption is discussed in Appendix C.

Goodness-of-fit is determined by calculation of a χ^2 from comparison of the experimental moments with those predicted by the results of the PWA fit. A systematic study has been performed to determine the effect on goodness-of-fit of adding and subtracting partial waves of $J \leq 2$ and $M \leq 1$. We find that although no significant structure is seen in the waves of negative reflectivity (see below), their presence in the PWA fit results in a significant improvement in goodness-of-fit compared to a fit which includes only the
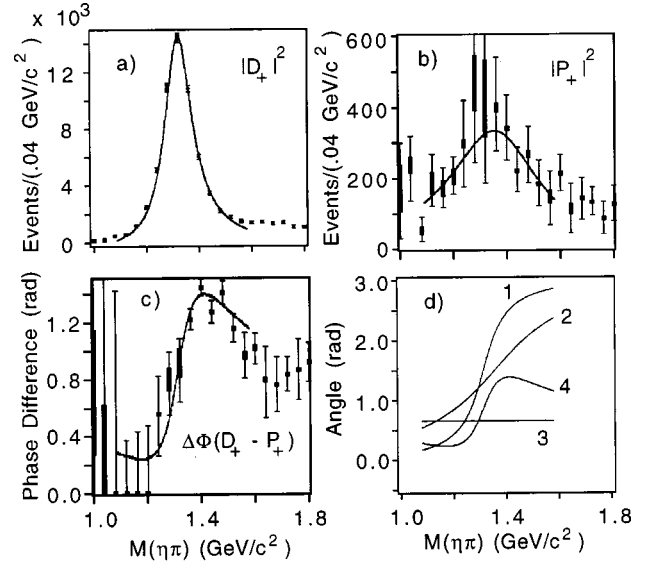

FIG. 17. Results of the partial wave amplitude analysis. Shown are (a) the fitted intensity distributions for the D_+ and (b) the P_+ partial waves, and (c) their phase difference $\Delta\Phi$. The range of values for the eight ambiguous solutions is shown by the central bar and the extent of the maximum error is shown by the error bars. Also shown as curves in (a), (b), and (c) are the results of the mass dependent analysis described in the text. The lines in (d) correspond to (1) the fitted D_+ Breit-Wigner phase, (2) the fitted P_+ Breit-Wigner phase, (3) the fitted relative production phase ϕ, and (4) the overall phase difference $\Delta\Phi$.

dominant positive-reflectivity partial waves. We have also performed fits including partial waves with $J=3$ and with $J=4$. Contributions from these partial waves are found to be within one standard deviation of zero for most mass bins with $M(\eta\pi^-) < 1.8$ GeV/c^2 and in all cases within two standard deviations of zero. Thus, PWA fits shown or referred to in this paper include all partial waves with $J \leq 2$ and $m \leq 1$ (i.e. S_0, P_0, P_-, D_0, D_-, P_+, and D_+). A non-interfering, isotropic background term of fixed magnitude determined as described by Method 2 in Sec. II D is used.

B. Results

The results of the PWA fit of 38,200 events in the range $0.98 < M(\eta\pi^-) < 1.82$ GeV/c^2 and $0.10 < |t| < 0.95$ (GeV/$c)^2$ are shown in Figs. 17 and 18. In Fig. 17 the acceptance-corrected numbers of events predicted by the PWA fit for the D_+ and P_+ intensities and the phase difference between these amplitudes, $\Delta\Phi$, are shown as a function of $M(\eta\pi^-)$. (The smooth curves shown in this figure are discussed below in Sec. V B.) There are eight ambiguous solutions in the fit [32,35,36]. These solutions are mathematically discrete but with equal likelihoods—that is, they correspond to exactly the same angular distributions. We show the range of fitted values for these ambiguous solutions in the vertical rectangular bar at each mass bin, and the maximum extent of their errors is shown as the error bar. These rectangular bars are quite small and thus not apparent for the
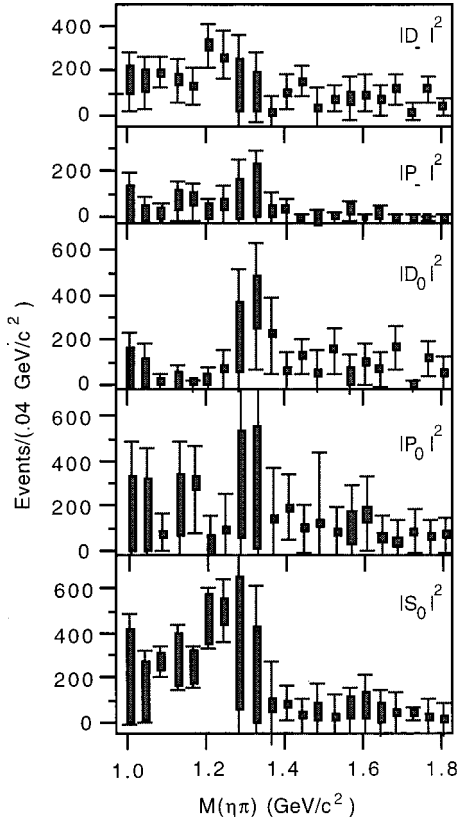
FIG. 18. Results of the partial wave amplitude analysis. Shown are the fitted intensity distributions for the waves produced by unnatural-parity exchange.
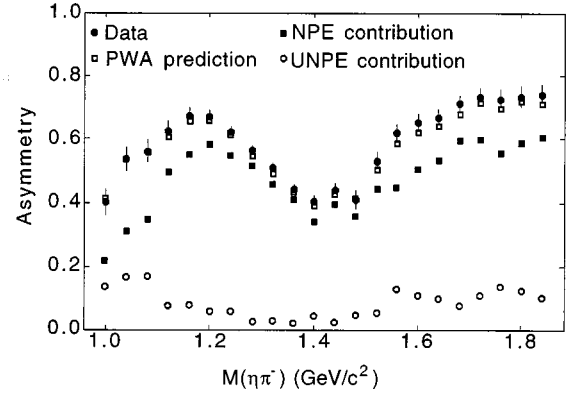

FIG. 19. Forward-backward asymmetry as a function of effective mass. Shown are: the total asymmetry in the data (closed circles); the predicted asymmetry from the PWA fit (open squares); the prediction of the fit for that part of the asymmetry due to natural-parity exchange (filled squares); and the prediction of the fit for that part of the asymmetry due to the unnatural-parity exchange waves (open circles).

D_+ intensity, but they are quite clear for the P_+-intensity and the phase-difference distributions.

The $a_2^-(1320)$ is clearly observed in the D_+ partial wave [Fig. 17(a)]. A broad peak is seen in the P_+ wave at about 1.4 GeV/c^2 [Fig. 17(b)]. The phase difference $\Delta\Phi$ increases through the $a_2^-(1320)$ region, and then decreases above about 1.5 GeV/c^2 [Fig. 17(c)]. This phase behavior will allow us to study the nature of the P_+ wave. (We note that there is a sign ambiguity in the phase difference and thus only the magnitude of $\Delta\Phi$ is actually measured.)

Shown in Fig. 18 are the fitted intensities for waves which are produced by negative-reflectivity (or unnatural-parity) exchange. The predicted numbers of events for these waves are generally small and are all consistent with zero above about 1.3 GeV/c^2. Although there is some non-zero contribution from the D_- and (especially) the S_0 waves below this region, the uncertainties and ambiguity ranges associated with these waves make it impossible to do a definitive study of them to determine their nature. In addition, the absence of a strong wave (such as the D_+ wave in the natural-parity sector) to beat against these waves precludes us from drawing any conclusions about possible resonant behavior in the unnatural parity sector.

The forward-backward asymmetry noted earlier is due to interference in the natural-parity exchange sector rather than to the unnatural-parity exchange waves. This is illustrated in Fig. 19 which shows the predicted asymmetry separately for

the natural and unnatural-parity exchange waves. It is clear that the asymmetry due to the unnatural-parity waves is about an order of magnitude less than that due to the natural-parity waves. Also shown in Fig. 19 is the comparison of the asymmetry present in the data with that predicted by the fit. The fit clearly does an excellent job in representing the data points.

The unnormalized spherical harmonic moments $H(LM)$ and their prediction from the PWA fit as a function of mass are shown in Fig. 20. Here $H(LM)=\Sigma_{i=1}^{N}Y_L^M(\theta_i,\phi_i)$ [N being the number of events in a given bin of $M(\eta\pi^-)$]. The relationships between the moments and the amplitudes are given in Appendix A, Eqs. (A27). All of the even moments ($M=0,2$) are well-described by the fit as are most of the $M=1$ moments. Some points with $M=1$ are somewhat less well fitted but, as we will discuss below, the significant conclusions which will be drawn from this work come from the natural-parity sector whose amplitudes do not contribute directly to the $M=1$ moments [see Eqs. (A27)].

An examination of the $H(30)$, $H(32)$, $H(40)$ and $H(42)$ moments along with a comparison with Eqs. (A27) shows that the D_+ amplitude dominates and demonstrates clearly that the P_+ partial wave is required for the PWA fit to describe the experimental moments. These moments cannot be described solely by the combination of the D_+ partial wave and experimental acceptance.

The change in $-\log(\text{Likelihood})$ as a function of the number of events for the P_+ partial wave for the 1.30 $<M(\eta\pi^-)<1.34$ GeV/c^2 bin is shown for all the ambiguous solutions in Fig. 21. The curves were obtained by fixing the P_+ intensity at various values and maximizing the likelihood function varying all of the other parameters. All eight ambiguous solutions were found for each value of the P_+ intensity. The number of predicted P_+ events at the maximum of the likelihood ranges from 330 events to 530 events for the eight solutions with typical errors of 280 events. [A change in $-\log(\text{Likelihood})$ of 0.5 corresponds to one standard deviation.] For all solutions, the likelihood function gets
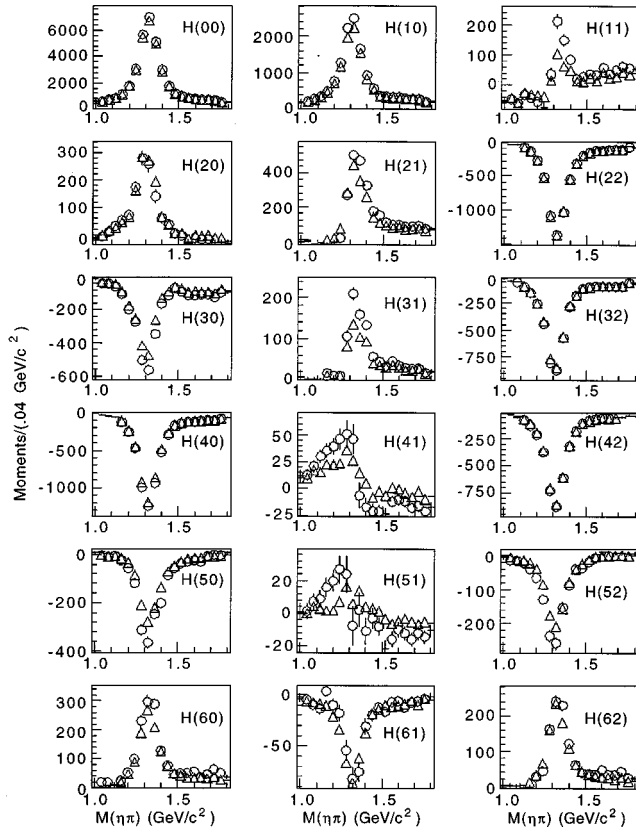
FIG. 20. Experimental moments $H(L,M)$ (open circles) shown with the predicted moments (open triangles) from the amplitude analysis.

so bad below 100 events that the P_+ wave is clearly required to fit the data. Thus the observed variation in $-\log(\text{Likelihood})$ further demonstrates that the P_+ partial wave is required to describe our data.
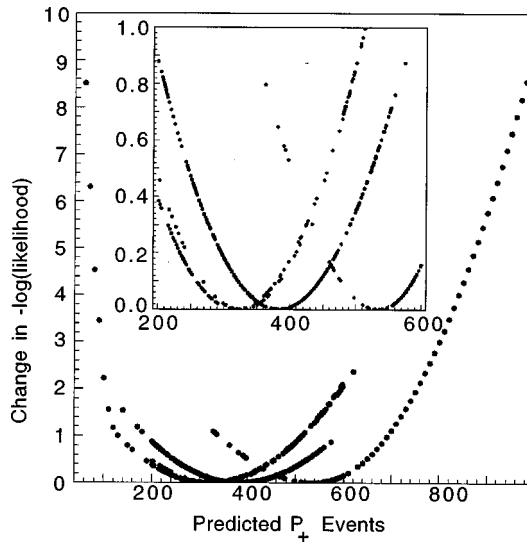

FIG. 21. Value of the log likelihood as a function of the number of P_+ events in the PWA fit for all 8 ambiguous solutions. The inset shows a view with expanded scales. Because some solutions are very close to each other, not all 8 solutions are distinguishable on this figure.
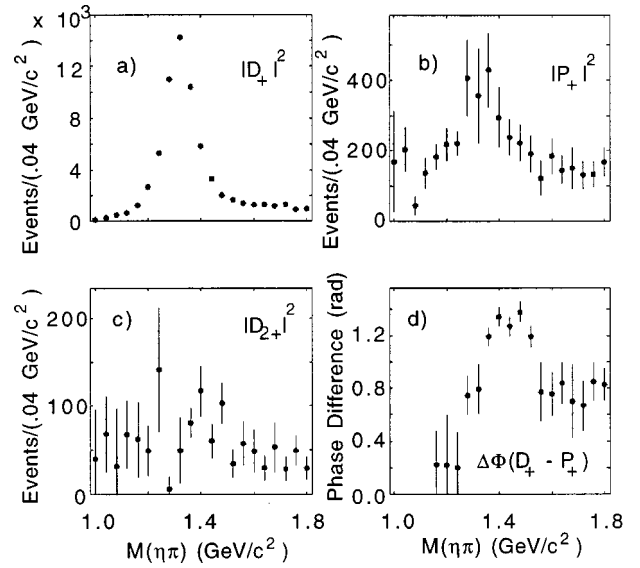

FIG. 22. Results of the partial wave amplitude analysis when the natural parity exchange $m=2$ amplitude is included. Shown are the fitted intensity distributions for (a) the D_+, (b) the P_+, and (d) the D_{2+} partial waves. Shown in (c) is the phase difference $\Delta\phi$ between the D_+ and the P_+ partial waves.

C. Systematic studies

PWA fits were performed for two different t ranges containing approximately equal numbers of events. One bin spanned the range $0.10 < |t| < 0.25$ $(\text{GeV}/c)^2$, and the other was for $0.25 < |t| < 0.95$ $(\text{GeV}/c)^2$. Both bins yielded comparable structures in the P_+ wave, and the $a_2^-(1320)$ was the dominant feature of the D_+ wave for both bins. The relative $P_+ - D_+$ phase behavior for each bin was similar to the results for the integrated fit shown in Fig. 17(c).

A PWA fit has been carried out excluding those events with $|\cos\theta_{GJ}| > 0.8$ (the region in which experimental acceptance is poorest). Neither the P_+-wave intensity nor its phase variation relative to the D_+ wave change by more than one standard deviation in any mass bin.

As mentioned above, a PWA fit has been carried out including the natural parity exchange $m=2$ amplitude (labeled D_{2+}) in the fit. The results of this fit are shown in Fig. 22. Comparing this fit with the fit shown in Fig. 17, it is clear that the magnitude and phase behavior of the P_+ wave is quite unaffected by inclusion of the $m=2$ amplitude.

To test for Δ and N^* contamination, a fit has been done in which events with $M(\pi^- p) < 2.0$ GeV/c^2 are excluded. As discussed earlier, the resulting intensities and phases did not change in most cases by more than one standard deviation and in no case by more than 1.5 standard deviations.

Fits were also carried out on Monte Carlo events generated with a pure D_+ wave to determine whether structure in the P_+ wave could be artificially induced by acceptance effects, resolution, or statistical fluctuations. Shown in Fig. 23 are the results of such a fit. We do find that a P_+ wave can be induced by such effects. This "leakage" leads to a P_+
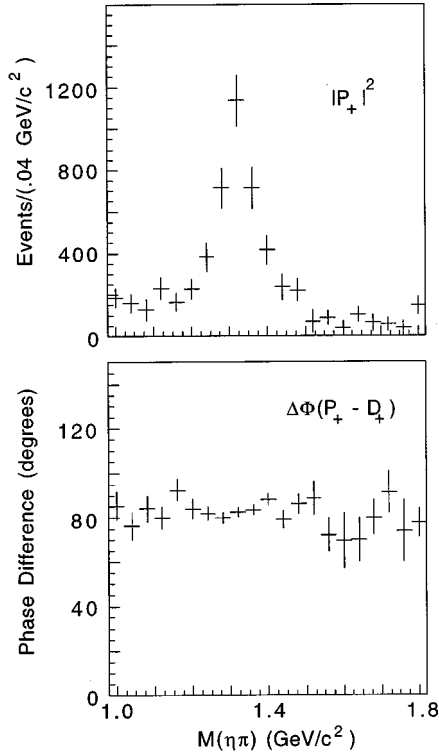
FIG. 23. Fitted P_+ intensity and $P_+ - D_+$ phase difference for the Monte Carlo sample generated with a pure D_+ sample of $a_2^-(1320)$ events.
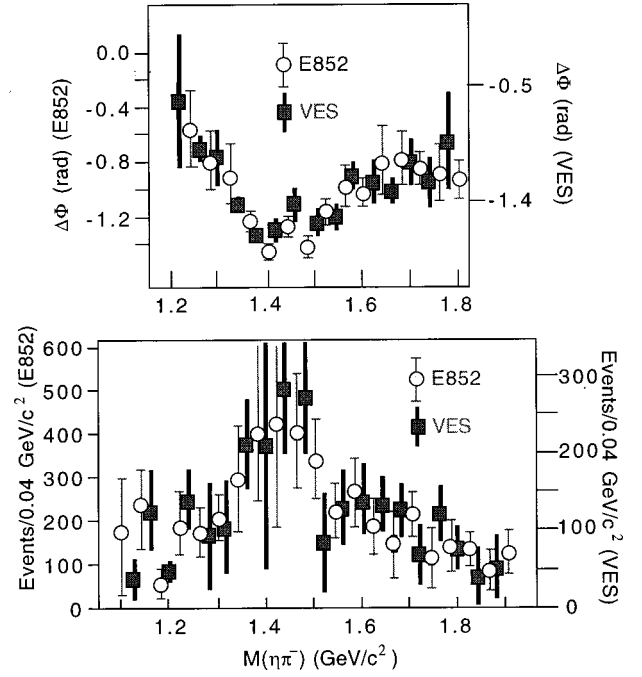

FIG. 24. Comparison of the results of this amplitude analysis with the VES experiment. Shown are the $P_+ - D_+$ phase difference and the P_+ intensity as a function of $\eta\pi^-$ effective mass for each experiment. Note that the left-hand scales are for E852 and the right-hand scales are for VES.

wave that (1) mimics the generated D_+ intensity [and in our case would therefore have the shape of the $a_2(1320)$]; and (2) has a phase difference $\Delta\Phi$ that is independent of mass. Neither property is present in our study and we conclude that the P_+ structure which we observe is not due to ''leakage.''

Fits have been performed allowing $l = 3$ and $l = 4$ waves. We find that these waves are negligible in the region below $M(\eta\pi^-)$ of about 1.7–1.8 GeV/c^2, their intensities being less than one standard deviation from zero in almost all bins. (The largest number of events in any bin for the F_+ wave was 34 ± 22 events and for the G_+ wave was 140 ± 100 events.)

The data have been fit using different parametrizations of the background. The background has been set at fixed values determined from the two different background estimates discussed previously. In another fit, the background has been set to zero. And finally, a fit was performed allowing the background level to be a free parameter. Although the negative reflectivity waves do change somewhat for different treatments of the background,[3] the results for the D_+ and P_+ waves and their relative phase do not change by more than one standard deviation in the entire region between 1.2 and 2.0 GeV/c^2 except for a few isolated points which vary up to 1.5 standard deviations.

D. Comparison with previous experiments

These results for the P_+ and D_+ intensities and their phase difference are quite consistent with the VES results [14] as can be seen in Fig. 24. In particular, the behavior of the shape of the phase difference is virtually identical to that reported by VES.[4] This is particularly noteworthy since, as will be seen below, it is this phase difference which allows us to draw conclusions regarding the nature of the P_+ wave.

Our results are compared with those of the KEK experiment [15] in Fig. 25. In this case, it is clear that the two results differ. The KEK results have a P-wave intensity which is narrower and a P-D phase difference which, within errors, is consistent with being constant as a function of $M(\eta\pi^-)$.

E. Comparison with $\eta \to \pi^+ \pi^- \pi^0$ data sample

A second data set in another topological class (with two additional charged particles in the final state) has been used to study Reaction (1) with the decay mode $\eta \to \pi^+\pi^-\pi^0$. Besides having three forward charged particles instead of one, these events have a π^0 instead of an η to be detected by the LGD. Since the π^0 is one of three pions in the η decay, its energy will be significantly less than the η in the topology

---

[3]Since the background and the S_0 wave are both isotropic, the fitting program cannot distinguish between them.

[4]The magnitude of the phase difference is shifted by about 20° relative to that of VES. A production phase shift would not be unexpected because of the differing energies and targets in the two experiments.

FIG. 27. The $\eta\pi^-$ effective mass distribution for the $\eta \rightarrow \pi^+\pi^-\pi^0$ event sample.
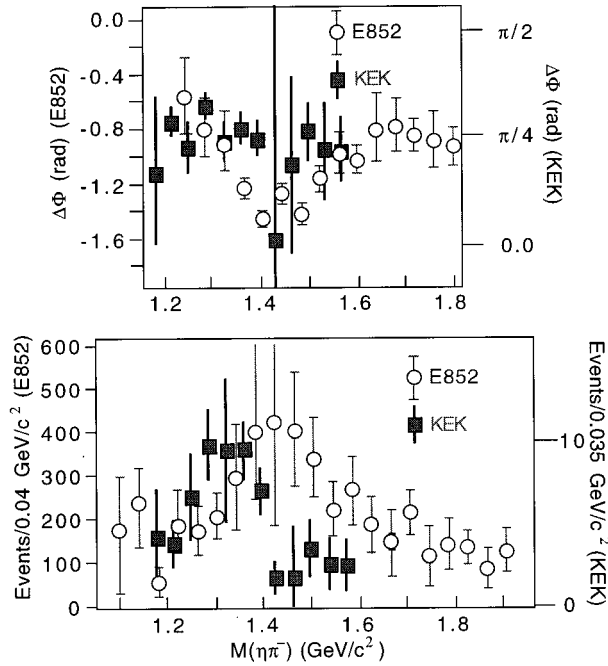
FIG. 25. Comparison of the results of this amplitude analysis with those of the KEK experiment. Shown are the $P_+ - D_+$ phase difference and the P_+ intensity as a function of $\eta\pi^-$ effective mass for each experiment. Note that the left-hand scales are for E852 and the right-hand scales are for KEK.

with only one charged track. Thus it is clear that the $\eta \rightarrow \pi^+\pi^-\pi^0$ data sample will have significantly different acceptance and systematics when compared to the $\eta \rightarrow 2\gamma$ sample.

Shown in Fig. 26 is the $\pi^+\pi^-\pi^0$ effective mass distribution from this data set. There is a clear η peak as well as a

strong peak in the ω region. After kinematic fitting, a sample was obtained of 2,235 events which were consistent with Reaction (1) with $\eta \rightarrow \pi^+\pi^-\pi^0$. Figure 27 shows the effective mass distribution for this sample of events. As expected, the $a_2^-(1320)$ dominates this spectrum.

Although the data sample is very small for this topology, we have carried out an amplitude analysis in order to compare with the primary $\eta \rightarrow 2\gamma$ analysis. Results of the analysis are shown in Fig. 28 where we compare the shapes of the P_+ intensities for the two data sets as well as the $P_+ - D_+$ phase differences. Despite the rather large statistical uncertainties, there is excellent agreement between these distributions.

V. MASS-DEPENDENT FIT

In an attempt to understand the nature of the P_+ wave observed in our experiment, we have carried out a mass-dependent fit to the results of the mass-independent amplitude analysis. The fit has been carried out in the $\eta\pi^-$ mass range from 1.1 to 1.6 GeV/c^2. In this fit, we have assumed that the D_+-wave and the P_+-wave decay amplitudes are resonant and have used relativistic Breit-Wigner forms for these amplitudes.

A. Procedure

We shall use a shorthand notation w to stand for the $\eta\pi^-$ mass, i.e. $w = M(\eta\pi^-)$. Representing the mass-dependent amplitudes for D_+ and P_+ as $V_l(w)$ for $l=2$ and 1, we may write

$$V_l(w) = e^{i\phi_l}\Delta_l(w)B_l(q)[a_l + b_l(w - w_l^0) + c_l(w - w_l^0)^2]^{1/2}$$
(2)

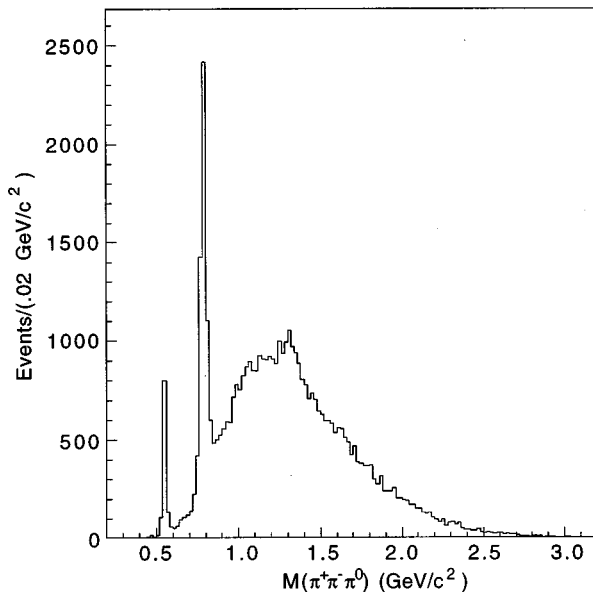where q is the $\eta\pi^-$ breakup momentum at mass w. Here ϕ_l

FIG. 26. The $\pi^+\pi^-\pi^0$ effective mass distribution for events with the topology of three forward charged tracks, one recoil charged track, and two photon clusters consistent with a π^0.
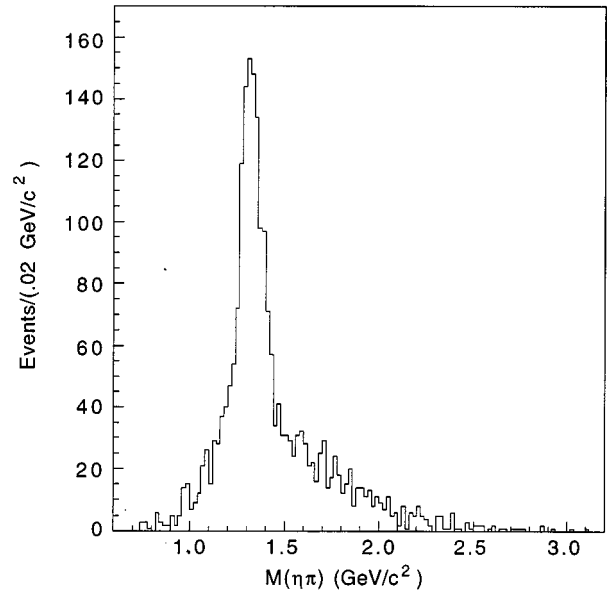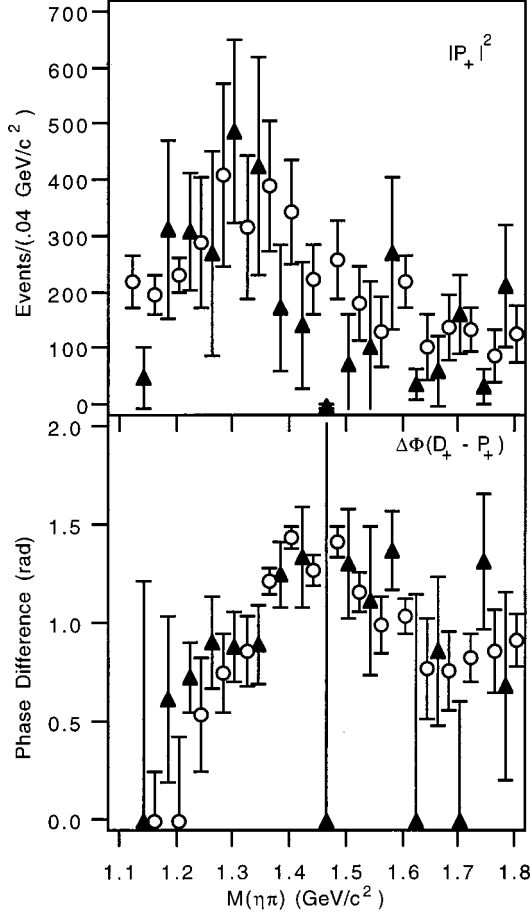
FIG. 28. Comparison of the results of the amplitude analysis for the $\eta \to \pi^+ \pi^- \pi^0$ (filled triangles) and the $\eta \to 2\gamma$ (open circles) samples. The ordinate scale for the P_+ intensity is for the $\eta \to 2\gamma$ fit only. Thus, only the shapes of the P_+ intensity distributions should be compared.

is the production phase (mass independent[5]) associated with a wave l. The quantities $\Delta_l(w)$ and $B_l(q)$ are the standard relativistic Breit-Wigner form and the barrier factor, respectively, and are given below. The square-root factor has been introduced primarily to take into account possible deviations from the standard Breit-Wigner form, at values of w away from the resonance mass (denoted by w_l^0). The overall normalization of a wave is governed by a_l, while the constants b_l and c_l allow for deviations in the mass spectra from the Breit-Wigner form. The constants a_l, b_l and c_l are all real, so that the square-root factor does not affect the rapidly varying phase implied by the standard Breit-Wigner form.[6]

The barrier functions [37], which are real, are given by

$$B_0(q)=1$$

$$B_1(q)=\left[\frac{z}{z+1}\right]^{1/2}$$

$$B_2(q)=\left[\frac{z^2}{(z-3)^2+9z}\right]^{1/2} \tag{3}$$

$$B_3(q)=\left[\frac{z^3}{z(z-15)^2+9(2z-5)}\right]^{1/2}$$

$$B_4(q)=\left[\frac{z^4}{(z^2-45z+105)^2+25z(2z-21)^2}\right]^{1/2}$$

where $z=(q/q_R)^2$ and $q_R=0.1973$ GeV/c corresponding to 1 fermi. Note that $B_l(q)\Rightarrow 1$ as $q\Rightarrow\infty$.

The relativistic Breit-Wigner functions can be written

$$\Delta_l(w)=\left[\frac{\Gamma_l^0}{\Gamma_l(w)}\right]e^{i\delta_l(w)}\sin\delta_l(w) \tag{4}$$

where Γ_l^0 is the nominal width (mass independent) and $\Gamma_l(w)$ is the mass-dependent width given by

$$\Gamma_l(w)=\Gamma_l^0\left(\frac{w_l^0}{w}\right)\left(\frac{q}{q_l^0}\right)\left[\frac{B_l(q)}{B_l(q_l^0)}\right]^2 \tag{5}$$

where q_l^0 is the breakup momentum evaluated at $w=w_l^0$. The mass-dependent phase shift $\delta_l(w)$ is given by

$$\cot\delta_l(w)=\left[\frac{w_l^0}{\Gamma_l(w)}\right]\left[1-\left(\frac{w}{w_l^0}\right)^2\right] \tag{6}$$

or

$$\cot\delta_l(w)=\left(\frac{w}{w_l^0}\right)\left(\frac{q_l^0}{q}\right)\left[\frac{B_l(q_l^0)}{B_l(q)}\right]^2\frac{(w_l^0)^2-(w)^2}{w_l^0\Gamma_l^0} \tag{7}$$

and the overall phase for the l-wave amplitude is

$$\Phi_l=\phi_l+\delta_l(w). \tag{8}$$

We are dealing with two waves, P_+ and D_+, and can only measure $\phi=\phi_2-\phi_1$. Thus the phase difference being measured experimentally, corresponds to

$$\Delta\Phi=\Phi_2-\Phi_1=\phi+\delta_2(w)-\delta_1(w). \tag{9}$$

Finally, the experimental mass distribution for each wave l is given by

$$\frac{d\sigma_l}{dw}=|V_l(w)|^2 pq \tag{10}$$

where pq is the phase-space factor for which p is the breakup momentum of the $\eta\pi^-$ system (or of the final-state proton) in the overall center-of-mass frame in Reaction (1). Since the problem here is for a given $\sqrt{s}$, all other relevant factors, including that of the beam flux, have been absorbed into the amplitude itself, i.e. the constants a_l, b_l and c_l.

---

[5]We have tried a linear dependence in mass for the production phase; the fits did not require it.

[6]For a Breit-Wigner form with a constant width, the phase rises 90 degrees over one full width centered at the resonance mass.

The input quantities to the fit included, in each mass bin: the P_+-wave intensity; the D_+-wave intensity; and the phase difference $\Delta\Phi$ [the relevant formulas are given in (9) and (10)]. Each of these quantities was taken with its error (including correlations) from the result of the amplitude analysis. One can view this fit as a test of the hypothesis that the correlation between the fitted P-wave intensity and its phase (as a function of mass) can be fit with a resonant Breit-Wigner amplitude.

We find that the fit does not improve significantly when the P_+ wave is modified from the Breit-Wigner form, and hence set b_1 and $c_1 = 0$ for the final fit. We also note that the magnitudes of the quantities b_2 and c_2 in the final fit correspond to a small deviation of the D_+-wave intensity of the order of 1%.

B. Results

Results of the fit are shown as the smooth curves in Figs. 17(a)–17(c). The mass and width of the $J^{PC} = 2^{++}$ state [Fig. 17(a)] are $(1317 \pm 1 \pm 2)$ MeV/c^2 and $(127 \pm 2 \pm 2)$ MeV/c^2 respectively [38]. (The first error given is statistical and the second is systematic.) The mass and width of the $J^{PC} = 1^{-+}$ state as shown in Fig. 17(b) are $(1370 \pm 16^{+50}_{-30})$ MeV/c^2 and $(385 \pm 40^{+65}_{-105})$ MeV/c^2 respectively. Shown in Fig. 17(d) are the Breit-Wigner phase dependences for the $a_2^-(1320)$ (line 1) and the P_+ waves (line 2); the fitted $D_+ - P_+$ production phase difference (line 3); and the fitted $D_+ - P_+$ phase difference (line 4). [Line 4, which is identical to the fitted curve shown in Fig. 17(c), is obtained as line 1 − line 2 + line 3.]

The systematic errors have been determined from consideration of the range of solutions possible because of the ambiguous solutions in the PWA. Since there are 8 ambiguous solutions per mass bin and we are fitting over 12 mass bins, it is clearly impossible to try all 8^{12} possible combinations. Instead, we have fit some 10^5 combinations where the values to be fitted in each mass bin have been chosen at random from among the 8 ambiguous PWA solutions. The resulting fits generally clump into a group with reasonable values of $\chi^2/\text{DOF} (\lesssim 2)$ and into a group with poor values. The systematic errors on the mass and width given above are taken from the extremes observed for the solutions with reasonable values of χ^2/DOF. The central values quoted above are taken from a fit which uses the average values of the input parameters in each bin.

The fit to the resonance hypothesis has a χ^2/DOF of 1.49. The fact that the production phase difference can be fit by a mass-independent constant (of 0.6 rad) is consistent with Regge-pole phenomenology[7] in the absence of final-state interactions. If one attempts to fit the data with a non-resonant (constant phase) P_+ wave, and also postulates a Gaussian intensity distribution for the P_+ wave, one obtains a very poor fit with a χ^2/DOF of 7.08. Finally if one allows a mass-dependent production phase, a χ^2/DOF of 1.55 is obtained

TABLE II. Comparison of the results of E852 and the Crystal Barrel for the parameters of the $J^{PC} = 1^{-+}$ resonance.

	Mass (MeV/c^2)	Width (MeV/c^2)
E852	$1370 \pm 16^{+50}_{-30}$	$385 \pm 40^{+65}_{-105}$
Crystal Barrel	$1400 \pm 20 \pm 20$	$310 \pm 50^{+50}_{-30}$

for the non-resonant hypothesis—but in this case the production phase must have a very rapid variation with mass.[8] Furthermore, for this non-resonant hypothesis, one must also explain the correlated structure observed in the P_+ intensity—a structure which is explained naturally by the resonance hypothesis.

An attempt [39] to explain our result as the interference of a non-resonant Deck-type background and a resonance at 1.6 GeV/c^2 can reproduce this correlation. (Evidence for an exotic meson with a mass near 1.6 GeV/c^2 has been reported [40] by our collaboration.) However, this explanation is excluded because of the recent observation [18] by the Crystal Barrel Collaboration which confirms the presence of this state produced in nucleon-antinucleon annihilation. The Deck-effect is a mechanism applicable to peripheral production but not to annihilation.

Our fitted parameters for the $J^{PC} = 1^{-+}$ resonance are compared in Table II with the values reported by the Crystal Barrel experiment [18]. That experiment reports that a $J^{PC} = 1^{-+}$ resonance in the $\eta\pi$ channel is required to fit their data in the annihilation channel $\bar{p}n \rightarrow \pi^-\pi^0\eta$. Their fitted parameters are very consistent with those determined from our mass-dependent analysis.

C. Other systematic studies

1. Sensitivity to the D-wave intensity distribution function

In order to determine the sensitivity of the results of our mass-dependent analysis to the exact function being used to fit the D-wave intensity distribution we have redone the fit using two other hypotheses. First we have performed a fit in which the mass-dependent amplitude is given by Eq. (2), but with $b_2 = c_2 = 0$. Second, we have taken $b_2 = c_2 = 0$ in Eq. (2) and also replaced the Blatt-Weisskopf barrier functions for each wave by the factor q^l. Although the resulting fits are poorer in quality, we find that the parameters of the fit do not change by amounts greater than the systematic uncertainty described above.

2. Sensitivity to leakage

As shown in Sec. IV C, the P_+ wave observed in our data is not consistent with ''leakage.'' That is, the analysis shows that the intensity and phase motion of the P_+ wave do not have the characteristics of the wave which is artificially generated from a pure D_+ wave due to possible incomplete knowledge of the resolution or detection inefficiency. This

---

[7]The signature factor and the residue functions are at most t-dependent (not mass dependent) (see Ref. [30]).

[8]The fit requires a linear production phase difference with a slope of -4.3 rad/GeV.

does not preclude the possibility of some leakage being present in the data and distorting the results of the mass dependent analysis (MDA). In this section, we describe a test which has been carried out to study the sensitivity of our MDA results to possible residual leakage being present in the data.

The fit which has been carried out is a mass dependent partial wave analysis (MDPWA). In such a fit, the PWA is carried out as in Section IV but instead of carrying it out separately for each $\eta\pi^-$ mass bin, all bins are fit simultaneously and are tied together with a mass-dependent function for each partial wave. That is, the extended maximum likelihood function of the form given by Eq. (B16) is generalized to include mass dependence:

$$\ln \mathcal{L} \propto \sum_{i}^{n} \ln I(\Omega_i, w_i) - \int d\Omega \, dw \, \eta(\Omega, w) I(\Omega, w). \tag{11}$$

The free parameters in the fit include, in addition to the amplitudes of the partial waves, the Breit-Wigner masses, widths, and intensities as well as mass-independent production amplitude phases.

For simplicity, we have taken the Breit-Wigner form of Eq. (2) to describe each of the partial waves. A common mass and width were used for the D_+, D_-, and D_0 partial waves. Similarly, the P_+, P_-, and P_0 waves were assumed to be described by a common mass and width. The S wave was assumed to have its own mass and width. The constants b_l and c_l of Eq. (2) were taken to be zero for the D_0, D_-, P_+, P_0, P_-, and S_0 waves. Each wave was allowed to have its own normalization constant and production phase.

In order to include leakage in the fit, a leakage amplitude P_+^{lk} with the characteristics obtained in the leakage study of Sec. IV C was defined. This amplitude was taken to have the shape of the D_+ amplitude as well as its Breit Wigner phase dependence. Its production phase was fixed at $\phi^{(lk)}=80°$. This amplitude was then combined coherently with the P_+ signal to given an effective amplitude given by the expression:

$$P_+^{(eff)}(w) = P_+(w) + P_+^{(lk)}(w) \tag{12}$$

where

$$P_+^{(lk)}(w) = a_1^{(lk)} e^{i\phi^{(lk)}} \Delta_2(w; w_2, \Gamma_2) B_2(q)$$
$$\times [1 + b_1^+(w - w_2^0) + b_2^+(w - w_2^0)^2]^{1/2}. \tag{13}$$

The results of the MDPWA fit are shown as the smooth curves in Fig. 29. Also shown as the points with error bars are the results of the mass-independent PWA. It is clear that the two analyses give consistent results. Shown in Fig. 29(a) are the P_+^{eff} intensity (curve 3) along with the P_+ signal intensity (curve 1). The leakage is shown in curve 2 as the sum of the leakage intensity and the (signal-leakage) interference term. The fitted leakage contribution is equal to $\mathcal{R}_l=0.018$ where we have defined
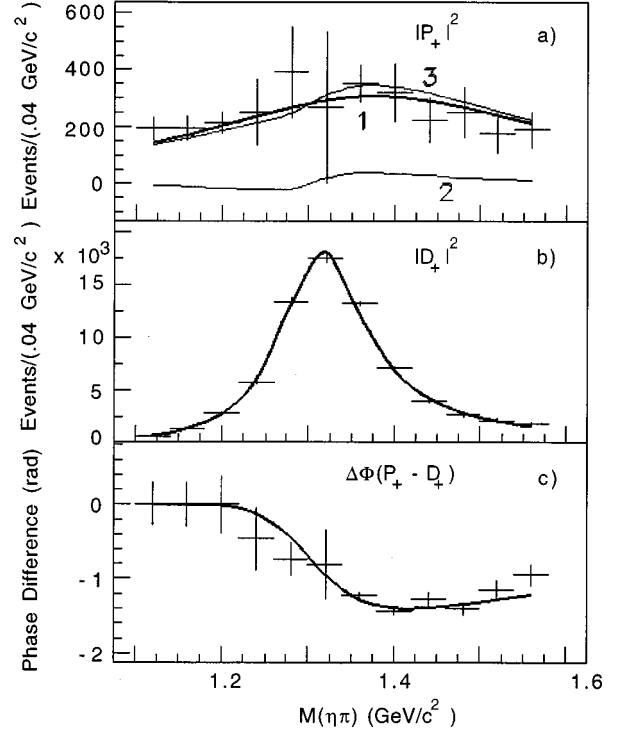

FIG. 29. The fit results of the MDPWA (curves) and of one solution for the mass independent PWA (crosses) for the $\eta\pi^-$ system: (a) P_+, (b) D_+ intensities and (c) their relative phase $\Delta\phi(P_+ - D_+)$. (a) also shows the contributions of the 1^{-+} signal intensity (1), the sum of the leakage and (signal-leakage) interference term (2) and the complete 1^{-+} wave (3).

$$\mathcal{R}_l = \left(\frac{a_1^{(lk)}}{a_2^+} \right). \tag{14}$$

The results of the fit are given in Table III where they are compared with those of the combined PWA and mass dependent fit. The results are quite compatible when one takes into account the systematic errors. The biggest difference is in the fitted width of the P_+ state which is larger for the MDPWA.

In Fig. 30 are shown the fitted values for the mass (curve 1) and the width (curve 2) of the 1^{-+} resonance as well as the change in $\ln \mathcal{L}$ as a function of $\mathcal{R}_l$ (the leakage fraction). We note that the mass and width are very insensitive up to values of $\mathcal{R}_l=5\%$, above which the fit becomes very unlikely.

TABLE III. Comparison of the results of the PWA combined with a separate mass dependent fit (MDF) with those of the MDPWA with leakage.

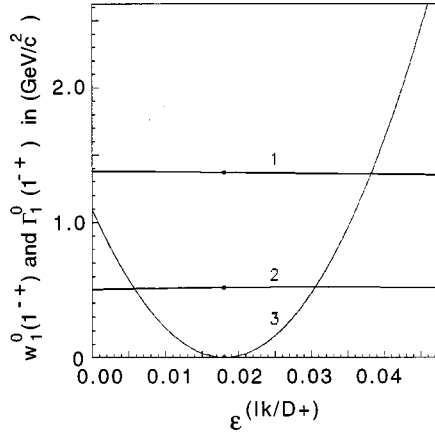| Meson		Mass (MeV/c^2)	Width (MeV/c^2)
$a_2^-(1320)$	E852 (PWA+MDF)	$1317\pm1\pm2$	$127\pm2\pm2$
	E852 (MDPWA)	1313 ± 1	119 ± 2
$\pi_1^-(1400)$	E852 (PWA+MDF)	$1370\pm16^{+50}_{-30}$	$385\pm40^{+65}_{-105}$
	E852 (MDPWA)	1369 ± 14	517 ± 40

FIG. 30. Dependence of the 1^{-+} signal parameters w_1^0 (1), Γ_1^0 (2) and the change in the $-\log(\text{Likelihood})$ function relative to its minimum (3) on the leakage contribution $\mathcal{R}_l$ at $\phi^{lk} = 80°$. The black points are at the position of the likelihood extremum.

D. Cross section estimate

In order to estimate the cross section for production of the observed P_+ state [which we now refer to as $\pi_1(1400)$], we have fitted published total cross sections [41–51] for $a_2^-(1320)$ production to a function of the form $\sigma = A(p/p_0)^{-n} + B$, where p is the beam momentum and p_0 is set to 1 GeV/c. Experiments with poor $a_1^-(1260)$/$a_2^-(1320)$ separation were excluded from the fit. The best fit gave: $A = 5099 \pm 221 \, \mu b$; $n = 1.88 \pm 0.03$; and $B = 39.2 \pm 2.0 \, \mu b$. From this we estimate the total cross section for $a_2^-(1320)$ production at 18.2 GeV/c to be $61.1 \pm 2.2 \, \mu b$. This is in good agreement with the result of $62.56 \pm 2.92 \, \mu b$ measured [47] at 18.8 GeV/c.

From the results of our PWA, we find that, in the $\eta\pi^-$ mass range from 1.10 to 1.58 GeV/c^2 there are $60{,}332 \pm 2{,}060$ D_+ events, and there are $3{,}321 \pm 1{,}245$ P_+ events. Here the error for the number of D_+ events is statistical and the error for the number of P_+ events includes uncertainties due to ambiguities. One thus obtains $\sigma(\pi^- p \rightarrow p\pi_1^-(1400)) * BR(\pi_1^-(1400) \rightarrow \eta\pi^-) = 0.49 \pm 0.19 \, \mu b$.

VI. SUMMARY AND CONCLUSIONS

In this paper, we have discussed the details of the amplitude analysis of data from Reaction (1). Interference between D-wave and P-wave amplitudes produced with natural parity exchange is required in order to explain the data. Using this interference, we have shown that the P-wave phase has a rapid variation with mass and that this phase variation coupled with the fitted P-wave intensity distribution is well-fitted by a Breit-Wigner resonance with mass and width of $(1370 \pm 16^{+50}_{-30})$ MeV/c^2 and $(385 \pm 40^{+65}_{-105})$ MeV/c^2 respectively. Since a P-wave resonance in the $\eta\pi$ system has $J^{PC} = 1^{-+}$, it is manifestly exotic. The exact nature of the observed state awaits further experimentation.

ACKNOWLEDGMENTS

APPENDIX A: PARTIAL-WAVE FORMULAS

In this appendix, the angular distributions are derived for the $\eta\pi^-$ system produced in Reaction (1). The distributions are given both in terms of the moments and the amplitudes in the reflectivity basis. For a system consisting of S, P and D waves, explicit formulas for the moments as functions of the partial waves are also given.

In the Gottfried-Jackson (GJ) frame, the amplitudes may be expanded in terms of the partial waves for the $\eta\pi^-$ system:

$$U_k(\Omega) = \sum_{lm} V_{lmk} A_{lm}(\Omega) \tag{A1}$$

where V_{lmk} stands for the production amplitude for a state $|lm\rangle$ and k represents the spin degrees of freedom for the initial and final nucleons ($k = 1, 2$ for spin-nonflip and spin-flip amplitudes). $A_{lm}(\Omega)$ is the decay amplitude given by

$$A_{lm}(\Omega) = \sqrt{\frac{2l+1}{4\pi}} D_{m0}^{l*}(\phi, \theta, 0) = Y_l^m(\Omega) \tag{A2}$$

where the angles $\Omega = (\theta, \phi)$ describe the direction of the η in the GJ frame. It is noted, in passing, that the small d-function implicit in (A2) is related to the associated Legendre polynomial via

$$d_{m0}^l(\theta) = (-)^m \sqrt{\frac{(l-m)!}{(l+m)!}} P_l^m(\cos\theta). \tag{A3}$$

The angular distribution is given by

$$I(\Omega) = \sum_k |U_k(\Omega)|^2. \tag{A4}$$

It should be emphasized that the nucleon helicities are external entities and the summation on k is applied to the absolute square of the amplitudes. A complete study of the $\eta\pi^-$ system requires four variables: $M(\eta\pi^-)$, $-t$ and the two angles in Ω. The distribution (A4) is therefore to be applied to a given bin of $M(\eta\pi^-)$ and of $-t$.

The angular distribution may be expanded in terms of the moments $H(LM)$ via

$$I(\Omega) = \sum_{LM} \left(\frac{2L+1}{4\pi}\right) H(LM) D_{M0}^{L*}(\phi, \theta, 0) \tag{A5}$$

where

$$H(LM)=\sum_{\substack{lm\\l'm'}}\left(\frac{2l'+1}{2l+1}\right)^{1/2}\rho_{mm'}^{ll'}(l'm'LM|lm)(l'0L0|l0)$$

$$(A6)$$

where ρ is the spin-density matrix given by

$$\rho_{mm'}^{ll'}=\sum_{k}V_{lmk}V_{l'm'k}^{*}.\qquad(A7)$$

It is seen that the moments $H(LM)$ are measurable quantities since

$$H(LM)=\int d\Omega I(\Omega)D_{M0}^{L}(\phi,\theta,0).\qquad(A8)$$

The normalization integral is

$$H(00)=\int d\Omega I(\Omega).\qquad(A9)$$

The symmetry relations for the H's are well-known. From the hermiticity of ρ, one gets

$$H^{*}(LM)=(-)^{M}H(L-M)\qquad(A10)$$

and, from parity conservation in the production process, one finds

$$H(LM)=(-)^{M}H(L-M).\qquad(A11)$$

These show that the H's are real.

Parity conservation in the production process can be treated with the reflection operator which preserves all the relevant momenta in the S-matrix and act directly on the rest states of the particles involved. It is important to remember that the coordinate system is always defined with the y-axis along the production normal. In this case the reflection operator is simply the parity operator followed by a rotation by π around the y-axis.

The eigenstates of this reflection operator are

$$|\epsilon lm\rangle=\theta(m)\{|lm\rangle-\epsilon(-)^{m}|l-m\rangle\}\qquad(A12)$$

where

$$\theta(m)=\frac{1}{\sqrt{2}},\quad m>0$$

$$=\frac{1}{2},\quad m=0\qquad(A13)$$

$$=0,\quad m<0.$$

For positive reflectivity, the $m=0$ states are not allowed: i.e.,

$$|\epsilon l0\rangle=0\quad\text{if}\quad\epsilon=+.\qquad(A14)$$

The reflectivity quantum number ϵ has been defined so that it coincides with the naturality of the exchanged particle in Reaction (1). One can prove this by noting that the meson

production vertex is in reality a time-reversed process in which a state of arbitrary spin-parity decays into a pion (the beam) and a particle of a given naturality (the exchanged particle)

$$J^{\eta_{J}}\to s^{\eta_{s}}+\pi\qquad(A15)$$

where η's stand for intrinsic parities. The helicity-coupling amplitude F^{J} for this decay [52] is

$$A_{p}^{J}(M)\propto F_{\lambda}^{J}D_{M\lambda}^{J*}(\phi_{p},\theta_{p},0)\qquad(A16)$$

where λ is the helicity of the exchanged particle and the subscript p stands for the "production" variables. M is the z-component of spin J in a J rest frame. From parity conservation in the decay, one finds

$$F_{\lambda}^{J}=-F_{-\lambda}^{J}\qquad(A17)$$

where one has used the relationships $\eta_{J}=(-)^{J}$ (true for two-pseudoscalar systems) and $\eta_{s}=(-)^{s}$ (natural-parity exchange). The formula shows that the helicity-coupling amplitude F^{J} is zero if λ is zero. Since angular momentum is conserved, its decay into two spinless particles in the final state cannot have $M=0$ along the beam direction (the GJ rest system), i.e. the D^{J}-function is zero unless $M=\lambda$, if $\theta_{p}=\phi_{p}=0$. Finally, one may identify J with l and M with m, which proves (A14).

The modified D-functions in the reflectivity basis are given by

$$^{\epsilon}D_{m0}^{l*}(\phi,\theta,0)=\theta(m)[D_{m0}^{l*}(\phi,\theta,0)-\epsilon(-)^{m}D_{-m0}^{l*}(\phi,\theta,0)].$$

$$(A18)$$

It is seen that the modified D-functions are real if $\epsilon=-1$ and imaginary if $\epsilon=+1$:

$$^{(-)}D_{m0}^{l*}(\phi,\theta,0)=2\theta(m)d_{m0}^{l}(\theta)\cos m\phi$$

$$^{(+)}D_{m0}^{l*}(\phi,\theta,0)=2i\theta(m)d_{m0}^{l}(\theta)\sin m\phi.\qquad(A19)$$

The overall amplitude in the reflectivity basis is now

$$^{\epsilon}U_{k}(\Omega)=\sum_{lm}{}^{\epsilon}V_{lmk}{}^{\epsilon}A_{lm}(\Omega)\qquad(A20)$$

where

$$^{\epsilon}A_{lm}(\Omega)=\sqrt{\frac{2l+1}{4\pi}}{}^{\epsilon}D_{m0}^{l*}(\phi,\theta,0)\qquad(A21)$$

and the resulting angular distribution is

$$I(\Omega)=\sum_{\epsilon k}|{}^{\epsilon}U_{k}(\Omega)|^{2}.\qquad(A22)$$

It is seen that the sum involves four non-interfering terms for $\epsilon=\pm$ and $k=1,2$. The absence of the interfering terms of different reflectivities is a direct consequence of parity conservation in the production process. We use the partial wave amplitude notation

$$[l]_{0}={}^{(-)}V_{l0},\quad[l]_{-}={}^{(-)}V_{l1},\quad[l]_{+}={}^{(+)}V_{l1}\qquad(A23)$$

where $[l]$ stands for the partial waves S, P, D, F and G for $l=0$, 1, 2, 3 and 4.

Consider an example where the maximum l is 2. One sees that there are in general twelve possible non-zero experimental moments:

$$H(00), \quad H(10), \quad H(11), \quad H(20), \quad H(21), \quad H(22)$$

$$H(30), \quad H(31), \quad H(32), \quad H(40), \quad H(41), \quad H(42) \tag{A24}$$

while the partial waves $[l]$ are, for unnatural-parity exchange,

$$S_0, \quad P_0, \quad P_-, \quad D_0, \quad D_- \tag{A25}$$

and, for natural-parity exchange,

$$P_+, \quad D_+. \tag{A26}$$

One wave in each naturality can be set be real (S_0 and P_+, for example), so that there are again twelve real parameters (to be determined). It is helpful to write down the moments explicitly in terms of the partial waves:

$$H(00) = S_0^2 + P_0^2 + P_-^2 + D_0^2 + D_-^2 + P_+^2 + D_+^2 \tag{A27}$$

$$H(10) = \frac{1}{\sqrt{3}} S_0 P_0 + \frac{2}{\sqrt{15}} P_0 D_0$$

$$+ \frac{1}{\sqrt{5}} (P_- D_- + P_+ D_+)$$

$$H(11) = \frac{1}{\sqrt{6}} S_0 P_- + \frac{1}{\sqrt{10}} P_0 D_- - \frac{1}{\sqrt{30}} P_- D_0$$

$$H(20) = \frac{1}{\sqrt{5}} S_0 D_0 + \frac{2}{5} P_0^2 - \frac{1}{5} (P_-^2 + P_+^2) + \frac{2}{7} D_0^2$$

$$+ \frac{1}{7} (D_-^2 + D_+^2)$$

$$H(21) = \frac{1}{\sqrt{10}} S_0 D_- + \frac{1}{5} \sqrt{\frac{3}{2}} P_0 P_- + \frac{1}{7\sqrt{2}} D_0 D_-$$

$$H(22) = \frac{1}{5} \sqrt{\frac{3}{2}} (P_-^2 - P_+^2) + \frac{1}{7} \sqrt{\frac{3}{2}} (D_-^2 - D_+^2)$$

$$H(30) = \frac{3}{7\sqrt{5}} (\sqrt{3} P_0 D_0 - P_- D_- - P_+ D_+)$$

$$H(31) = \frac{1}{7} \sqrt{\frac{3}{5}} (2 P_0 D_- + \sqrt{3} P_- D_0)$$

$$H(32) = \frac{1}{7} \sqrt{\frac{3}{2}} (P_- D_- - P_+ D_+)$$

$$H(40) = \frac{2}{7} D_0^2 - \frac{4}{21} (D_-^2 + D_+^2)$$

$$H(41) = \frac{1}{7} \sqrt{\frac{5}{3}} D_0 D_-$$

$$H(42) = \frac{\sqrt{10}}{21} (D_-^2 - D_+^2).$$

APPENDIX B: MAXIMUM-LIKELIHOOD ANALYSIS

This appendix is devoted to an exposition of the experimental moments, the acceptance moments and the acceptance-corrected (or ''true'') moments and the relationships among them. Finally, the extended likelihood functions are given as functions of the ''true'' and acceptance moments.

One may determine directly the experimental moments (unnormalized) as follows:

$$H_x(LM) = \sum_i^n D_{M0}^L(\phi_i, \theta_i, 0) \tag{B1}$$

where the sum is over a given number n of experimental events in a mass bin. But this is given by, from (A8),

$$H_x(LM) = \int d\Omega \, \eta(\Omega) I(\Omega) D_{M0}^L(\phi, \theta, 0) \tag{B2}$$

where $\eta(\Omega)$ represents the finite acceptance of the apparatus, and includes software cuts, if any. From (A5), one finds that

$$H_x(LM) = \sum_{L'M'} H(L'M') \Psi_x(LML'M') \tag{B3}$$

where

$$\Psi_x(LML'M') = \left(\frac{2L'+1}{4\pi} \right) \int d\Omega \, \eta(\Omega)$$

$$\times D_{M0}^L(\phi, \theta, 0) D_{M'0}^{L'*}(\phi, \theta, 0). \tag{B4}$$

Note that the Ψ's have a simple normalization

$$\Psi_x(LML'M') = \delta_{LL'} \delta_{MM'} \tag{B5}$$

in the limit $\eta(\Omega)=1$. The integral (B4) can be calculated using a sample of ''accepted'' Monte Carlo (MC) events. Let N_x be the number of accepted MC events, out of a total of N generated MC events. Then, the integral is

$$\Psi_x(LML'M') = \left(\frac{2L'+1}{4\pi} \right) \frac{1}{N}$$

$$\times \sum_i^{N_x} D_{M0}^L(\phi_i, \theta_i, 0) D_{M'0}^{L'*}(\phi_i, \theta_i, 0). \tag{B6}$$

Equation (B3) shows that one can predict the experimentally measurable moments (B1), given a set of true moments $\{H\}$ and the Ψ's; this provides one a means of assessing the goodness of fit by forming a χ^2 based on the set $\{H_x\}$.

There exists an alternative method of determining Ψ's. For the purpose, one expands the acceptance function $\eta(\Omega)$ in terms of the orthonormal D-functions, as follows:

$$\eta(\Omega)=\sum_{LM}(2L+1)\xi(LM)D^{L*}_{M0}(\phi,\theta,0) \qquad (B7)$$

where $\xi(LM)$ is given by

$$\xi(LM)=\frac{1}{4\pi}\int d\Omega\,\eta(\Omega)D^{L}_{M0}(\phi,\theta,0). \qquad (B8)$$

The complex conjugate is, from the defining formula above,

$$\xi^*(LM)=(-)^M\xi(L-M) \qquad (B9)$$

so that the acceptance function can be made explicitly real

$$\eta(\Omega)=\sum_{LM}(2L+1)\tau(M)\mathrm{Re}\{\xi(LM)D^{L*}_{M0}(\phi,\theta,0)\} \qquad (B10)$$

where

$$\tau(M)=2,\quad M>0,$$
$$=1,\quad M=0,$$
$$=0,\quad M<0. \qquad (B11)$$

One sees that $\tau(M)=4\theta^2(M)$ where $\theta(M)$ is defined in Eq. (A13).

A set of $\xi(LM)$ specifies completely the acceptance in the problem. The normalization for the acceptance function has been chosen so that a perfect acceptance is given by $\eta(\Omega)=1$ and $\xi(LM)=\delta_{L0}\delta_{M0}$. The $\xi(LM)$'s can be measured experimentally using the accepted MC events

$$\xi(LM)=\frac{1}{4\pi N}\sum_{i}^{N_x}D^{L}_{M0}(\phi_i,\theta_i,0). \qquad (B12)$$

Finally, substituting (B7) into (B4), one finds

$$\Psi_x(LML'M')=\sum_{L''M''}(2L''+1)\xi^*(L''M'')$$
$$\times(LML''M''|L'M')(L0L''0|L'0). \qquad (B13)$$

This formula shows an important aspect of the $\xi(LM)$ technique of representing acceptance. Although (B8) involves a sum in which L and M could be extended to infinity for an arbitrary acceptance, there is a cutoff if the set $\{H\}$ has maxima L_m and M_m [see (B3)]. The formula above demonstrates that $L''\leq 2L_m$ and $|M''|\leq 2M_m$.

In a partial-wave analysis, it is usually best to take a set of the partial waves, $[l]_0$, $[l]_-$ and $[l]_+$, as unknown parameters to be determined in an extended maximum-likelihood fit. Since there is an absolute scale in an extended maximum-likelihood fit, one then has the predicted numbers of events

for all the partial waves, corrected for finite acceptance and angular distributions. The partial waves in turn give rise to a set of predicted moments $\{H\}$. But the $H(00)$ is not 1 but the total predicted number of events from the fit, i.e. one should be using the unnormalized moments. It is possible to choose H's as unknowns in the fit, but the two sets of H's should be the same ideally—this affords one an effective way of assessing self-consistency between the chosen moments and the partial waves.

For completeness, a short comment is given about the extended likelihood functions. The likelihood function for finding n events in a given bin with a finite acceptance $\eta(\Omega)$ is defined as a product of the probabilities,

$$\mathcal{L}\propto\left[\frac{\bar{n}^n}{n!}e^{-\bar{n}}\right]\prod_{i}^{n}\left[\frac{I(\Omega_i)}{\int I(\Omega)\,\eta(\Omega)d\Omega}\right] \qquad (B14)$$

where the first bracket is the Poisson probability for n events. This is the so-called extended likelihood function, in the sense that the Poisson distribution for n itself is included in the likelihood function. Note that the expectation value $\bar{n}$ for n is given by

$$\bar{n}\propto\int I(\Omega)\,\eta(\Omega)d\Omega. \qquad (B15)$$

The likelihood function $\mathcal{L}$ can now be written, dropping the factors depending on n alone,

$$\mathcal{L}\propto\left[\prod_{i}^{n}I(\Omega_i)\right]\exp\left[-\int I(\Omega)\,\eta(\Omega)d\Omega\right].$$

The "log" of the likelihood function now has the form,

$$\ln\mathcal{L}\propto\sum_{i}^{n}\ln I(\Omega_i)-\int d\Omega\,\eta(\Omega)I(\Omega) \qquad (B16)$$

which can be recast in terms of the $\xi(LM)$'s

$$\ln\mathcal{L}\propto\sum_{i}^{n}\ln I(\Omega_i)-\sum_{LM}(2L+1)H(LM)\xi^*(LM)$$
$$\propto\sum_{i}^{n}\ln I(\Omega_i)-\sum_{LM}(2L+1)\tau(M)H(LM)\mathrm{Re}\,\xi(LM). \qquad (B17)$$

$H(LM)$'s may be used directly as parameters in the fit or may be given as functions of the partial waves. It is interesting to note that the $\xi(LM)$'s for $L>L_m$ and $|M|>M_m$ are not needed in the likelihood fit. Note also that only the real parts of the $\xi(LM)$'s are used in the fit.

It should be borne in mind that a set of the moments $\{H\}$ may not always be expressed in terms of the partial waves. This is clear if one examines the formulas (A27). Consider, for example, an angular distribution in which $H(10)$ is the only non-zero moment. But this moment is given by a set of interference terms involving even-odd partial waves. So at least one term cannot be zero—for example, the interference

term involving S- and P-waves. But then neither $H(00)$ nor $H(20)$ can be zero, since both S- and P-waves are non-zero. One must conclude then that a χ^2 based on the set $\{H_x\}$ may not necessarily be zero identically.

APPENDIX C: RANK OF THE DENSITY MATRIX

An assumption needed for the partial-wave analysis is that the density matrix has rank 1, i.e. the spin amplitudes do not depend on the nucleon helicities. Our justification, so far, has been that the fitted partial waves are very reasonable, that these waves can be fitted with a very simple mass-dependent formula, that Pomeron-exchange amplitudes are in general independent of nucleon helicities, and so on . . . .

The purpose of this appendix is to point out that, under a simple model for mass dependence of the partial waves, it is possible to prove that the spin density matrix has rank 1. Suppose that one has found a satisfactory fit under a rank-1 assumption. One can then show that, even if the problem involves both spin-nonflip and spin-flip at the nucleon vertex—i.e. it appears to be a rank-2 problem—the spin density matrix in reality has a rank of 1. Although this note is based on the results of our $\eta\pi^-$ analysis, the derivation does not depend on the decay channels; the conclusions apply equally well to other decay channels.

This note relies on some technicalities generally well known, and so they have been presented without attribution. The reader may wish to consult a number of preprints and/or papers, which deal with them in some detail [31,34,52–54].

1. Partial waves produced via natural-parity exchange

Consider the $\eta\pi^-$ system produced via natural-parity exchange. It consists mainly of just two waves D_+ and P_+ in the $a_2^-(1320)$ region. Assume these are the only waves. Without loss of generality, the decay amplitudes [32] can be considered real, i.e.

$$A_D(\Omega) = \sqrt{\frac{5}{4\pi}}\sqrt{2}d_{10}^2(\theta)\sin\phi$$

$$= -\sqrt{\frac{5}{4\pi}}\sqrt{3}\sin\theta\cos\theta\sin\phi$$

$$A_P(\Omega) = \sqrt{\frac{3}{4\pi}}\sqrt{2}d_{10}^1(\theta)\sin\phi$$

$$= -\sqrt{\frac{3}{4\pi}}\sin\theta\sin\phi. \tag{C1}$$

Since one deals with the partial waves produced only by natural-parity exchange, one can drop the subscript "+" from the waves, and the angular distribution is simply given by

$$I(\Omega) \propto |DA_D(\Omega) + PA_P(\Omega)|^2 \propto \left(\frac{3}{4\pi}\right)|\sqrt{5}D\cos\theta$$

$$+ P|^2\sin^2\theta\sin^2\phi \propto \left(\frac{3}{4\pi}\right)[5|D|^2\cos^2\theta$$

$$+ 2\sqrt{5}\Re\{D^*P\}\cos\theta + |P|^2]\sin^2\theta\sin^2\phi. \tag{C2}$$

The integration over the angles can be carried out easily, to obtain

$$\int I(\Omega)d\Omega \propto |D|^2 + |P|^2 \tag{C3}$$

as expected.

It is easy to calculate the forward-backward asymmetry $A(F,B) = (F-B)/(F+B)$ (see Sec. III)

$$A(F,B) = \frac{3\sqrt{5}}{4}\cos(\Delta\Phi)\frac{|P||D|}{(|P|^2 + |D|^2)} \tag{C4}$$

where $\Delta\Phi$ is the phase difference between the P and D waves.

The spin density matrix is given by

$$I(\Omega) \propto |DA_D(\Omega) + PA_P(\Omega)|^2 = \sum_{k,k'}\rho_{k,k'}A_kA_{k'}^* \tag{C5}$$

where $\{k,k'\} = \{1,2\}$ and "1" ("2") corresponds to D (P). From this definition, one sees that

$$\rho = \begin{pmatrix} |D|^2 & DP^* \\ D^*P & |P|^2 \end{pmatrix}. \tag{C6}$$

One can work out the eigenvalues of this 2×2 matrix:

$$\lambda = \{|D|^2 + |P|^2, 0\}. \tag{C7}$$

One of the two allowed eigenvalues is zero, i.e. the rank of this matrix is 1. This is the "rank-1" assumption one makes to carry out the partial-wave analysis and is valid for a given mass bin.

Suppose now that the rank is 2, i.e.

$$I(\Omega) \propto |D_1A_D(\Omega) + P_1A_P(\Omega)|^2 + |D_2A_D(\Omega) + P_2A_P(\Omega)|^2 \tag{C8}$$

where subscripts 1 and 2 stand for spin-nonflip and spin-flip amplitudes at the nucleon vertex for Reaction (1). Comparing (C2) and (C8), one finds immediately

$$|D|^2 = |D_1|^2 + |D_2|^2$$

$$|P|^2 = |P_1|^2 + |P_2|^2 \tag{C9}$$

$$\Re\{P^*D\} = \Re\{P_1^*D_1\} + \Re\{P_2^*D_2\}.$$

Let w be the effective mass of the $\eta\pi^-$ system. If the mass dependence is included explicitly in the formula, one should write, in the case of rank 1,

$$\frac{d\sigma(w,\Omega)}{dwd\Omega} \propto |D(w)A_D(\Omega) + P(w)A_P(\Omega)|^2 pq \tag{C10}$$

where p is the breakup momentum of the $\eta\pi^-$ system in the overall c.m. system and q is the breakup momentum of the η in the $\eta\pi^-$ rest frame. Note that both p and q depend on w. Note also that the w dependences of the partial waves D and

P are given in the formula. Obviously, a similar expression could be written down for the case of rank 2.

One is now ready to make the one crucial assumption for a mass-dependent analysis of the D and P waves: one assumes that two resonances—in D and P waves, respectively— are produced in both spin-nonflip and spin-flip amplitudes. One may then write, for the rank-1 case,

$$D(w) = a e^{i\alpha} e^{i\delta_a} \sin \delta_a$$
$$P(w) = b e^{i\delta_b} \sin \delta_b$$

(C11)

where a, b and the production phase α are all real and independent of the $\eta\pi^-$ mass. In addition, one can set $a \geq 0$ and $b \geq 0$ without loss of generality. Here δ_a and δ_b are the phase-shifts corresponding to the resonances and are highly mass dependent. In its generic form, the Breit-Wigner formula is given by the usual expression

$$\cot \delta = \frac{w_0^2 - w^2}{w_0 \Gamma_0}$$

(C12)

where w_0 and Γ_0 are the standard resonance parameters. In this note, the width is considered independent of w. Likewise, the barrier factor dependence for D and P is ignored.[9]

The formulas (C11) are generalized to the case of rank 2, as follows:

$$D_1(w) = a_1 e^{i\alpha_1} e^{i\delta_a} \sin \delta_a$$
$$P_1(w) = b_1 e^{i\delta_b} \sin \delta_b$$
$$D_2(w) = a_2 e^{i\alpha_2} e^{i\delta_a} \sin \delta_a$$
$$P_2(w) = b_2 e^{i\delta_b} \sin \delta_b.$$

(C13)

Once again, a_i, b_i and α_i are real, $a_i \geq 0$ and $b_i \geq 0$, and independent of w. One finds, using (C9),

$$a^2 = a_1^2 + a_2^2$$
$$b^2 = b_1^2 + b_2^2$$

(C14)

$$ab \cos(\alpha + \delta_a - \delta_b) = a_1 b_1 \cos(\alpha_1 + \delta_a - \delta_b)$$
$$+ a_2 b_2 \cos(\alpha_2 + \delta_a - \delta_b).$$

A plot of $\cos(\alpha + \delta_a - \delta_b)$ as a function of w is shown in Fig. 31 for three values of α, i.e. 0°, 45° and 90°. The resonance

FIG. 31. $\cos(\alpha + \delta_a - \delta_b)$ as a function of w from 1.2 to 1.6 GeV/c^2 for $\alpha = 0°$ ($\diamond$), $\alpha = 45°$ (+) and $\alpha = 90°$ ($\square$).

parameters for a and b of 1.0 and 0.151 are taken from the mass dependent fit of Section V B as are the resonant masses and widths.[10] The normalized absolute squares of the Breit-Wigner forms are given in Fig. 32, as is the "normalized" interference term. The same quantities, as they appear in Ref. [1], are shown in Fig. 33. This figure shows how important the interference term is compared to the P-wave term. Note also how rapidly the interference term varies as a function of w in the $a_2(1320)$ region. This term, of course, is intimately related to the asymmetry in the Jackson angle and vanishes when integrated over the angle, i.e. it does not contribute to the mass spectrum [see (C2) and (C3)]. Figure 34 shows the contour plot of the intensity distribution in w vs. $\cos \theta$; note the variation of the asymmetry as a function w.

For the last equation in (C14) to be true for any mass, the coefficient of $\cos(\delta_a - \delta_b)$ or $\sin(\delta_a - \delta_b)$ on the left-hand side must be equal to that on the right-hand side, so that

$$ab \cos \alpha = a_1 b_1 \cos \alpha_1 + a_2 b_2 \cos \alpha_2$$
$$ab \sin \alpha = a_1 b_1 \sin \alpha_1 + a_2 b_2 \sin \alpha_2.$$

(C15)

Taking the sum of the squares of the two formulas above and introducing the first two equations of (C14), one obtains:

FIG. 32. $\sin^2 \delta_a$ ($\diamond$), $\sin^2 \delta_b$ (+) and $\sin \delta_a \sin \delta_b \cos(\alpha + \delta_a - \delta_b)$ ($\square$) as a function of w from 1.2 to 1.6 GeV/c^2, using $\alpha = 45°$.

----

[9]Although simplified formulas are used in this article, the results given here do not change even when correct formulas are used. Note that, to go over to a correct formulation for each wave, one needs to substitute the absolute value of the Breit-Wigner formula as follows:

$$\sin \delta(w) \rightarrow \rightarrow B(q) \left[\frac{\Gamma_0}{\Gamma(w)} \right] \sin \delta(w)$$

where $B(q)$ is the barrier factor and $\Gamma(w)$ is the mass-dependent width. It should be noted that the correction factors are all real, by definition.
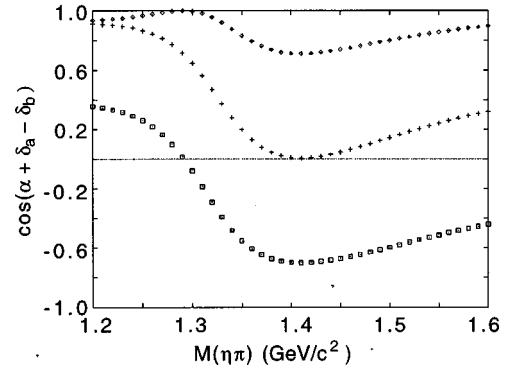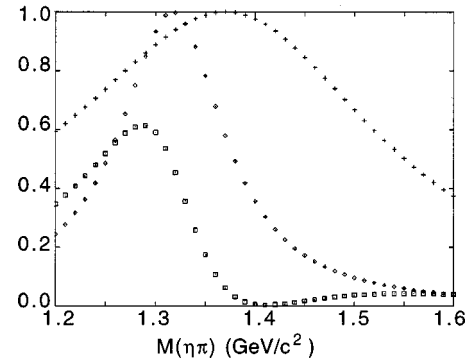
----

[10]The value of α as determined from this fit is 37.46°; for the purpose of illustration, one may consider $\alpha = 45°$ close enough.
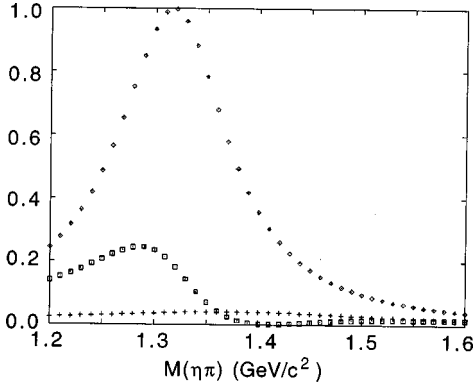
FIG. 33. $a^2 \sin^2 \delta_a$ ($\diamond$), $b^2 \sin^2 \delta_b$ (+) and $2ab \sin \delta_a \sin \delta_b \cos(\alpha + \delta_a - \delta_b)$ ($\square$) as a function of w from 1.2 to 1.6 GeV/c^2, where one has assumed that $a = 1.0$, $b = 0.20$ and $\alpha = 45°$.

$$2a_1b_1a_2b_2 \cos \alpha_1 \cos \alpha_2 + 2a_1b_1a_2b_2 \sin \alpha_1 \sin \alpha_2$$

$$= a_1^2 b_2^2 + a_2^2 b_1^2 = a_1^2 b_2^2 (\cos^2 \alpha_1 + \sin^2 \alpha_1)$$

$$+ a_2^2 b_1^2 (\cos^2 \alpha_2 + \sin^2 \alpha_2) \quad \text{(C16)}$$

which is recast into

$$0 = (a_1 b_2 \cos \alpha_1 - a_2 b_1 \cos \alpha_2)^2 + (a_1 b_2 \sin \alpha_1$$

$$- a_2 b_1 \sin \alpha_2)^2. \quad \text{(C17)}$$

It is clear that each term must be set to zero, so that

$$\left(\frac{a_1}{b_1}\right) \cos \alpha_1 = \left(\frac{a_2}{b_2}\right) \cos \alpha_2$$

$$\left(\frac{a_1}{b_1}\right) \sin \alpha_1 = \left(\frac{a_2}{b_2}\right) \sin \alpha_2. \quad \text{(C18)}$$

Placing these back into (C15), one deduces that

$$\left(\frac{a}{b}\right) \cos \alpha = \left(\frac{a_1}{b_1}\right) \cos \alpha_1 = \left(\frac{a_2}{b_2}\right) \cos \alpha_2$$

$$\left(\frac{a}{b}\right) \sin \alpha = \left(\frac{a_1}{b_1}\right) \sin \alpha_1 = \left(\frac{a_2}{b_2}\right) \sin \alpha_2. \quad \text{(C19)}$$

One may take—alternately—the sum of the squares of the two formulas above, or a division of the second by the first, and obtain (remembering that the a's and b's are non-negative real quantities),

$$\frac{a}{b} = \frac{a_1}{b_1} = \frac{a_2}{b_2}$$

$$\tan \alpha = \tan \alpha_1 = \tan \alpha_2. \quad \text{(C20)}$$

The last equation above demands that α_1 and α_2 are determined (up to $\pm \pi$), but they have to satisfy (C19). It is therefore clear that one must set $\alpha = \alpha_1 = \alpha_2$. Next, one introduces two new real variables $x \geq 0$ and $y \geq 0$, given by
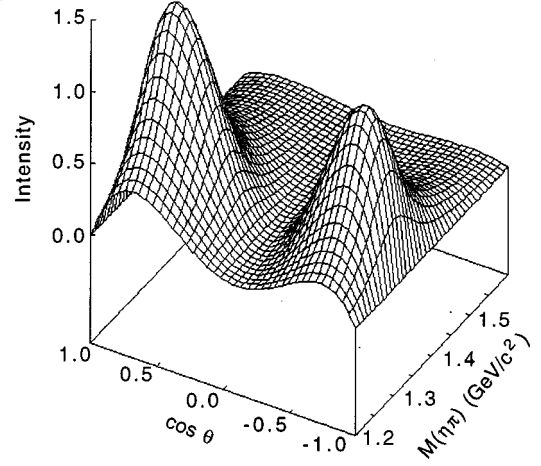

FIG. 34. Angular distribution in $\cos \theta$ as a function of w from 1.2 to 1.6 GeV/c^2, where one has assumed that $a = 1.0$, $b = 0.151$ and $\alpha = 37.46°$.

$$x = \frac{a_1}{a} = \frac{b_1}{b}$$

$$y = \frac{a_2}{a} = \frac{b_2}{b} \quad \text{(C21)}$$

with the constraint $x^2 + y^2 = 1$.

Now one can prove that the case of rank 2 is reduced to that of rank 1. Indeed, one sees immediately that

$$\begin{pmatrix} D_1 \\ P_1 \end{pmatrix} = x \begin{pmatrix} D \\ P \end{pmatrix} \quad \text{and} \quad \begin{pmatrix} D_2 \\ P_2 \end{pmatrix} = y \begin{pmatrix} D \\ P \end{pmatrix} \quad \text{(C22)}$$

and (C8) becomes identical to (C2).

2. Discussion

It is shown in this appendix that the problem of two resonances in D_+ and P_+ in the $\eta \pi^-$ system in (1) is—effectively—a rank-1 problem. For this to be true, the following conditions have to be met:

(a) There exist two distinct resonances with different masses and/or widths. Note that the crucial step, from (C14) to (C15), depends on that fact that $\delta_a - \delta_b$ is non-zero and is mass dependent.

(b) There exists a satisfactory rank-1 fit with two resonances in a given mass region, in which each amplitude for D_+ or P_+ has the following general form

$$\mathcal{M}_k(w, \Omega) = r_k e^{i\alpha_k} e^{i\delta_k(w)} f_k(w) A_k(\Omega) \quad \text{(C23)}$$

where $k = \{1, 2\}$ and "1" ("2") corresponds to D_+ (P_+). $\delta_k(w)$ is the Breit-Wigner phase and highly mass dependent, while r_k and α_k are mass independent in the fit. Of course, one of the two α_k's can be set to zero without loss of generality, so that there are three independent parameters, e.g. r_1, r_2 and α_1 (these were denoted a, b and α, respectively, in the previous section). $f_k(w)$ contains the absolute value of the Breit-Wigner form, plus any other mass-dependent fac-

tors introduced in the model. $A_k(\Omega)$ carries the information about the rotational property of a partial wave k.

(c) The same two D_+ and P_+ resonances are produced in both spin-nonflip and spin-flip amplitudes, with the same general form as given above—but with arbitrary r_k's and α_k's for each spin-nonflip and spin-flip amplitude. It has been shown in this appendix that only one set of r_k's and α_k's, i.e. r_1, r_2 and α_1, is required for both spin-nonflip and spin-flip amplitudes. (This is indeed a remarkable result; the rank-2 problem entails a set of six parameters, but it has been shown that the set is reduced to that consisting of just three.) Therefore, the distribution function in both w and Ω is given by

$$\frac{d\sigma(w,\Omega)}{dw\,d\Omega} \propto \left| \sum_k \mathcal{M}_k(w,\Omega) \right|^2 pq \qquad \text{(C24)}$$

independent of the nucleon helicities.

In other words, the spin density matrix has rank 1. The key ingredients for this result are that both spin-nonflip and spin-flip amplitudes harbor two resonances in D_+ and P_+ and that the production phase is mass-independent. It should be emphasized that the derivation given in this article does not depend on the existence of a good mass fit; it merely states that any fit with a mass-independent production phase is necessarily a rank-1 fit. Of course, the point is moot, if there exists no satisfactory fit in this model.

---

[1] D. R. Thompson *et al.*, Phys. Rev. Lett. **79**, 1630 (1997).

[2] N. Isgur and J. Paton, Phys. Rev. D **31**, 2910 (1985).

[3] F. de Viron and J. Ewyers, Nucl. Phys. **B185**, 391 (1981).

[4] T. Barnes and F. E. Close, Phys. Lett. **116B**, 365 (1982).

[5] M. Chanowitz and S. Sharpe, Nucl. Phys. **B222**, 211 (1983).

[6] T. Barnes *et al.*, Nucl. Phys. **B224**, 241 (1983).

[7] F. E. Close and P. R. Page, Nucl. Phys. **B443**, 233 (1995).

[8] T. Barnes, F. E. Close, and E. S. Swanson, Phys. Rev. D **52**, 5242 (1995).

[9] R. L. Jaffe, Phys. Rev. D **15**, 267 (1977).

[10] I. I. Balitsky, D. I. Dyakonov, and A. V. Yung, Z. Phys. C **33**, 265 (1986); J. I. Latorre, P. Pascual, and S. Narison, *ibid.* **34**, 347 (1987); J. Govaerts *et al.*, Nucl. Phys. **B262**, 575 (1985).

[11] Y. Uehara *et al.*, Nucl. Phys. **A606**, 357 (1996).

[12] P. Lacock, C. Michael, P. Boyle, and P. Rowland, Phys. Rev. D **54**, 6997 (1996); C. Bernard *et al.*, Nucl. Phys. B (Proc. Suppl.) **53**, 228 (1997).

[13] D. Alde *et al.*, Phys. Lett. B **205**, 397 (1988).

[14] G. M. Beladidze *et al.*, Phys. Lett. B **313**, 276 (1993).

[15] H. Aoyagi *et al.*, Phys. Lett. B **314**, 246 (1993).

[16] C. Amsler *et al.*, Phys. Lett. B **333**, 277 (1994).

[17] Y. D. Prokoshkin and S. A. Sadovsky, Yad. Fiz. **58**, 662 (1995) [Phys. At. Nucl. **58**, 606 (1995)].

[18] W. Dünnweber *et al.*, in *Proceedings of the Seventh International Conference on Hadron Spectroscopy*, edited by Suh-Urk Chung and Hans J. Willutzki, AIP Conf. Proc. No. 432 (AIP, New York, 1997), p. 309; A. Abele *et al.*, Phys. Lett. B **423**, 175 (1998).

[19] S. Ozaki, ''Abbreviated Description of the MPS,'' Brookhaven MPS note 40 (1978).

[20] Z. Bar-Yam *et al.*, Nucl. Instrum. Methods Phys. Res. A **386**, 235 (1997).

[21] T. Adams *et al.*, Nucl. Instrum. Methods Phys. Res. A **368**, 617 (1996).

[22] S. E. Eiseman *et al.*, Nucl. Instrum. Methods Phys. Res. **217**, 140 (1983).

[23] R. R. Crittenden *et al.*, Nucl. Instrum. Methods Phys. Res. A **387**, 377 (1997).

[24] S. Teige *et al.*, in *Proceedings of the Fifth International Conference on Calorimetry in High Energy Physics*, edited by Howard A. Gordon and Doris Rueger (World Scientific, Singapore, 1995), p. 161. See also S. Teige *et al.*, Phys. Rev. D **59**, 012001 (1999).

[25] O. I. Dahl *et al.*, ''SQUAW kinematic fitting program,'' Univ. of California, Berkeley Group A programming note P-126 (1968).

[26] J. Friedman, ''SAGE, A General System for Monte Carlo Event Generation with Preferred Phase Space Density Distributions,'' Univ. of California, Berkeley Group A programming note P-189 (1971).

[27] ''GEANT Detector Description and Simulation Tool,'' CERN program Library Long Writeups Q123 (1993).

[28] E. J. Sacharidis, Lett. Nuovo Cimento **25**, 193 (1979).

[29] M. Margulies *et al.*, Phys. Rev. D **14**, 667 (1976).

[30] A. C. Irving and R. P. Worden, Phys. Rep., Phys. Lett. **34C**, 117 (1977).

[31] S. U. Chung, ''Formulas for Partial-Wave Analysis,'' Brookhaven BNL-QGS-93-05 (1993).

[32] S. U. Chung, Phys. Rev. D **56**, 7299 (1997).

[33] J. P. Cummings and D. W. Weygand, ''The New BNL Partial Wave Analysis Program,'' Brookhaven Report BNL-64637 (1997).

[34] The naturality of the exchanged particle is given by the reflectivity of the wave. See S. U. Chung and T. L. Trueman, Phys. Rev. D **11**, 633 (1975).

[35] S. A. Sadovsky, ''On the Ambiguities in the Partial-Wave Analysis of $\pi^- p \to \eta \pi^0 n$ Reaction,'' Inst. for High Energy Physics IHEP-91-75 (1991).

[36] E. Barrelet, Nuovo Cimento A **8**, 331 (1972).

[37] F. v. Hippel and C. Quigg, Phys. Rev. D **5**, 624 (1972).

[38] This mass and width are consistent with accepted values for the $a_2(1320)$ [R. M. Barnett *et al.*, Phys. Rev. D **54**, 1 (1996)] when our resolution is taken into account.

[39] A. Donnachie and P. R. Page, Phys. Rev. D **58**, 114012 (1998).

[40] G. S. Adams *et al.*, Phys. Rev. Lett. **81**, 5760 (1998).

[41] V. Flaminio *et al.*, CERN, High Energy React. Anal. Group (Rep.) **83-01**, 238 (1983).

[42] M. J. Losty *et al.*, Phys. Lett. **56B**, 96 (1975).

[43] G. V. Beketov *et al.*, Yad. Fiz. **13**, 765 (1971) [Sov. J. Nucl. Phys. **13**, 435 (1971)].

[44] A. D. Johnson *et al.*, Phys. Rev. D **7**, 1314 (1973).

[45] G. Thompson *et al.*, Nucl. Phys. **B101**, 285 (1975).

[46] A. D. Martin *et al.*, Phys. Lett. **74B**, 417 (1978).

[47] V. Chabaud *et al.*, Nucl. Phys. **B145**, 349 (1978).

[48] C. Evangelista *et al.*, Nucl. Phys. **B178**, 197 (1981).

[49] T. Kitagaki *et al.*, Phys. Rev. D **26**, 1554 (1982).

[50] C. Bromberg *et al.*, Phys. Rev. D **29**, 2469 (1984).

[51] W. E. Cleland *et al.*, Nucl. Phys. **B208**, 228 (1982).

[52] S. U. Chung, ''Spin Formalisms,'' CERN Yellow Report CERN 71-8 (1971).

[53] S. U. Chung, Phys. Rev. D **48**, 1225 (1993).

[54] S. U. Chung *et al.*, Ann. Phys. (Leipzig) **4**, 404 (1995).